NASA Technical Memorandum 81248

Experimental Study of Supersonic Viscous Leeside Flow Over a Slender Delta Wing

Joachim Szodruch

December 1980

National Aeronautics and
Space Administration

NASA Technical Memorandum 81248

Experimental Study of Supersonic Viscous Leeside Flow Over a Slender Delta Wing

Joachim Szodruch, Ames Research Center, Moffett Field, California

National Aeronautics and
Space Administration

Ames Research Center
Moffett Field, California 94035

LIST OF SYMBOLS

A1	primary attachment line
A2	secondary attachment line, etc.
L	model length
M_∞	free-stream Mach number
M_N	Mach number component normal to the leading edge
P_T	total pressure
R_{L_∞}	Reynolds number based on free-stream conditions and model length
T_T	total temperature
S,S1	primary separation line
S2	secondary separation line, etc.
s	half-span of wing
x	axial distance from wing apex
y	spanwise distance from centerline
α	angle of attack
α_N	angle of attack in a plane normal to the leading edge

EXPERIMENTAL STUDY OF SUPERSONIC VISCOUS LEESIDE FLOW OVER A SLENDER DELTA WING

Joachim Szodruch*

Ames Research Center

SUMMARY

An investigation was conducted to study, in detail, the vortical flow over the leeward side of a 70° swept delta wing having subsonic and supersonic leading edges. Two types of flow were encountered and studied in detail, namely leading-edge separation and separation with a shock. Especially for the latter type, Reynolds number plays an important role and unexpected strong streamwise vortices were observed. An optical method is described to obtain a first approximation of shear stress values in the streamwise direction across the wing span.

INTRODUCTION

Vortices are one of the main characteristics of the flow around delta wings. The origin, location, and form of the vortices depend on many parameters such as Mach number, Reynolds number, sweep angle, angle of attack, and form of the leading edge. Figure 1 shows one way of describing and systematizing the vortical flow fields over the leeward side of a delta wing in supersonic flow. A detailed discussion about the different types of flow and the validity of the α_N vs M_N diagram is given in reference 1.

Since there seems to be a lack of data for critical assessment of computations, this study was the first part of a detailed investigation about the leeward vortical flow about a delta wing in supersonic flow to support and improve computational methods for calculating these flow fields. As shown in figure 1, the trajectory of experimental conditions runs along the left and right of the Stanbrook-Squire boundary which separates attached and detached flow at the leading edge. The experiments carried out were flow visualization studies, static pressure, and shear stress measurements.

The author wishes to thank J. G. Marvin for help in preparing this report and M. Kussoy for help and discussions during the experiments.

---

*National Research Council Associate.

MODEL AND APPARATUS

The model was a 70° swept delta wing with straight and sharp leading edges. The upper surface is flat; the cross-sectional shape is triangular with an angle of 25° between upper and lower surface. The overall length of the model is L = 20.7 cm (8.15 in.); the maximum half-span is then S = 7.5 cm (2.97 in.). As seen in figure 2, the model and strut support are combined into one piece. Two models were built: one for flow visualization, the other having pressure orifices at different spanwise and chordwise locations. Figure 3 shows the model, including the angle of attack mechanism and parts of the test section.

The wind tunnel used was the High Reynolds Number Channel I at Ames Research Center. The tunnel is a blowdown facility designed for operation up to reservoir pressures of 500 psi. Two new rectangular M = 2 and 3 nozzles were built for the investigation. The test section size is 25.4 × 38.1 cm (10 × 15 in.). A list of actual Mach and Reynolds numbers based on model chord length is given in table I. The intention was to achieve as high a

TABLE I.- MACH AND REYNOLDS NUMBER VARIATION [T_T ~ 278° K (500° R)]

Nominal Mach number, M	Actual Mach number, M_∞	Total pressure, P_T[psia]	Reynolds number, R_{L_∞}
2	1.90	3.0	0.6×10^6
	1.95	10.3	2.1×10^6
	1.98	130.0	25×10^6
3	2.75	17.0	2.1×10^6
	2.98	211.0	25×10^6

Reynolds number factor as possible. The lower total pressures were limited by choking conditions and by stability of the flow. The maximum pressure values are dictated by the loading on windows in the test section.

RESULTS AND DISCUSSION

The first series of tests was carried out at the nominal Mach number M = 2. As seen in figure 1, the experimental trajectory is completely within the region with leading-edge separation. A first indication about the type and extent of the vortical flow is given by Schlieren and oil-flow visualization tests. In figures 4(a) and (b) Schlieren photographs for angles of attack α = 0°, 5°, and 8°, and two Reynolds numbers show the height of the vortex above the wing. Note that vortices develop already at α = 0° since the angle of attack is measured with respect to the upper surface. Thus, the

lower surface is still at angle of attack and there is flow around the leading edge. At angles of attack higher than $\alpha = 8°$ breakdown of the flow occurs, induced by a detached shock wave from the strut support of the delta wing (see fig. 5).

The oil-flow visualization in figure 6 indicates the expected flow type of leading-edge separation. At $\alpha = 0°$ streamwise vortices are present originating from the leading edge and interfering with the oil trace of the primary vortex. The flow then develops in a continuous way until, at $\alpha = 8°$, two separation lines, secondary and tertiary, are present, while of course, the leading edge forms the primary separation line. In the centerline region, attached flow is seen and the primary attachment line can be defined. Essentially the same flow pattern is recognized for the high Reynolds number case in figure 7. Also, because of the h'gher shear, the vortex skin-friction line pattern and the separation lines are more distinct than at lower Reynolds numbers. The strut interference pattern on the leeward side and the trace of the detached strut support shock wave on the windward side at higher angles of attack are shown in the oil-flow results in figure 8. Note that despite the vortex breakdown on the rear of the wing, the forward part still shows undisturbed flow and all measurements there are considered valid.

For further flow visualization in supersonic flow the vapor screen method was used (fig. 2). A liquid, usually water (in this test a mixture of 2 ℓ alcohol, 200 mℓ water, and 10 mℓ latex), is sprayed into the settling chamber. Passing the liquid through the nozzle forms a light fog in the test section. It is uniformally distributed unless there are disturbances in the flow, induced by the presence of a model, for example. If a thin sheet of light illuminates a cross section of the model, vortex formation might be visible. The test arrangement for the present experiments is shown in figure 9. The vapor screen was hardly visible with the eye, so exposure times of $5 = 40$ sec are typical for the following pictures. Note that in all vapor-screen pictures the model is inverted, that is, the leeward surface is on the lower side. The result for $M = 2$ and angle of attack $\alpha = 5°$ is presented in the photograph in figure 10(a). Due to the viewing angle, the vortex closest to the camera has the best resolution. A reconstructed view in the flow direction is shown with primary attachment lines and secondary separation lines from oil-flow visualization, which indicate good agreement with the vapor screen.

In figure 10(b) the vapor-screen photograph at $\alpha = 8°$ exhibits, besides the primary vortex, traces of the secondary vortex underneath the primary one, as well as part of the bow shock wave. The reconstructed view in the flow direction combined with results from oil-flow and Schlieren visualization is shown on the right side of the figure.

Flow visualization results give an idea about the location of the vortex in the flow field and about attachment and separation lines on the leeward surface. The upper diagram in figure 11 presents the movement of the secondary separation line with angle of attack for the two Reynolds numbers. Since the flow underneath the primary vortex withstands separation longer at the high Reynolds number, secondary separation lines are further outboard, as the

experiment shows. The lower diagram in figure 11 indicates the "flattening" of the vortices as the Reynolds number increases for angle of attack to 10°. In addition, figures 12(a) and 12(b) give the primary vortex position on the leeward side for $R_{L_\infty} = 2 \times 10^6$ and 25×10^6, respectively. Arrows on the surface indicate the positions of the primary attachment lines. Due to symmetry, only half of the delta wing is shown.

When the Mach number is increased to $M_\infty = 3$, the type of flow over the leeward side is expected to change according to the trajectory in figure 1. The flow might be detached at or near the leading edge, and embedded shock waves are likely to be present. Again Schlieren and oil-flow photographs are presented first to locate the main features of the leeward flow field. Schlieren visualization of the delta wing at angle of attack is shown in figures 13(a) and 13(b) for low and high Reynolds numbers, respectively. Note that the visible Mach waves in the test section do not seem to influence the flow field around the delta wing as confirmed by pressure measurements. The oil-flow visualization over the leeward side for $M_\infty = 3$, $R_{L_\infty} = 2 \times 10^6$, and various other angles of attack reveals the difference from the case with leading-edge separation (see figures 14(a)-(d)). At low angles of attack, strong streamwise vortices (refs. 3 and 4) develop and interfere with the primary vortex on a larger scale than seen at $M_\infty = 2$. These streamwise vortices are still present in the cross flow at higher angles of attack (probably up to $\alpha = 10°$) weakening the skin-friction line pattern of the primary vortex in the rear part of the wing (see especially $\alpha = 5°$).

Figures 15(a)-(f) show close-up pictures for the tip region (60% of the chord length). Noteworthy at $\alpha = 7°$ is a turbulence spot in the attached flow region about the plane of symmetry. At $\alpha = 8°$ some leading-edge roughness induces a rather strong vortex which interacts downstream with the primary vortex. Furthermore, at $\alpha = 9°$ nearly conical lines appear in the outboard part of the wing. It is interesting that the skin-friction pattern running into these lines can be associated with a vortex of the same rotational sense as the primary one. The oil-flow visualization in figures 16(a)-(f) has been caried out at the higher Reynolds number $R_{L_\infty} = 25 \times 10^6$. Up to angles of attack $\alpha = 5°$ these are streamwise vortices, not only within the region about the plane of symmetry, but also within the inboard flow about or near the leading edge. At angles of attack higher than $\alpha = 5°$ the streamwise vortices in the crossflow become stronger and influence the entire skin-friction pattern outboard of the region of the primary vortex. A closer view of the skin-friction pattern in the tip region at the above conditions is given in figures 17(a)-(f). Interestingly, in the very tip region (typically 0.5% of the chord length) vortex-free flow exists (see also ref. 1). To complete the flow visualization, vapor-screen pictures are presented using the same test arrangement as in figure 9. These tests were performed at two angles of attack and two Reynolds numbers and results are in figures 18(a)-(d), supported by results from oil-flow and Schlieren experiments. At $\alpha = 5°$ and a low Reynolds number, a flat vortex region is found, originating at or close to the leading edge (see fig. 18(a)). As the Reynolds number is increased to $R_{L_\infty} = 25 \times 10^6$ (fig. 18(b)), a white region inboard of the wing

appears. So far in the presentation of vapor-screen visualization only vortices have been considered which separate at the leading edge. Thus, little condensated vapor will get into the vortex, and dark regions appear on the photograph. If it is assumed that inboard shock induced separation occurs, condensated vapor is getting around the leading edge and might be concentrated in the vortex, as indicated in figure 18(b). At the higher angle of attack $\alpha = 8°$, but low Reynolds number, again a flat vortex region appears which separates at or near to the leading edge (see fig. 18(c)). If the Reynolds number is increased, regions with concentrated vapor again appear, indicating shock-induced separation (see fig. 18(d)). These results and conclusions are consistent with the flow fields and their boundaries, as seen in the α_N vs M_N diagram in figure 1.

Results of the flow visualization at $M_\infty = 3$ and the two different Reynolds numbers are presented in a compressed form in figures 19 and 20. Separation lines and the height of the primary vortex above the wing are plotted in figure 19. The definition of the separation lines (upper diagram in fig. 19) was not easily discernable at either low angles of attack ($\alpha = 0°$ to 5°) for the low Reynolds number or at higher angles of attack ($\alpha = 5°$ to 9°) for the higher Reynolds number. The sudden change of separation-line position at high Reynolds numbers was consistent with the crossing of the flow boundaries in figure 1. However, the position of the primary vortex was obtained for all angles of attack and Reynolds numbers (see figs. 20(a) and 20(b)). Again, as was the case with leading-edge separation, it was observed, at low angles of attack, that the primary vortex center lies closer to the surface and moves inboard as the Reynolds number increases. Szodruch and Peak (ref. 1) discussed the dependence of the type of flow "separation with shock" (see fig. 1) on the Reynolds number and found that, for high Reynolds number, this type of flow vanishes. Figure 21 shows that results of the present experiments are consistent with the discussion in reference 1.

Mainly to support the computational results and, to a lesser degree, to improve the physical understanding of the flow, static pressure measurements on the leeward side of the delta wing at angle of attack and different Reynolds numbers were obtained. The three planes of measurement are shown in figure 22. Since some computational results are already available for a similar delta wing (75° sweep) at $M_\infty = 1.95$, $\alpha = 10°$, and $R_{L_\infty} = 0.7 \times 10^6$, some static-pressure measurements were carried out at the low Reynolds number $R_{L_\infty} = 0.6 \times 10^6$ (see figs. 23(a)-(c)). Unfortunately, at the higher angles of attack, strut interference influenced over 50% of the wing upstream of the trailing edge (see fig. 23(a)), where the pressure distribution is plotted along a conical line in the outboard part of the wing. At a chordwise station $x/L = 0.65$, only angles of attack up to $\alpha = 6°$ give undisturbed results. Figure 23(c) shows the theoretical (ref. 5) and experimental pressure distribution. The chordwise station $x/L = 0.2$, even at $\alpha = 10°$, is not influenced by the strut interference and allows a comparison between theory and experiment (see fig. 23(b)). Note that the computations so far only allow laminar flow results. Also, theoretical velocity plots in a cross sectional plane exhibit no attached region about the centerline; however, secondary separation might be encountered. At the higher Reynolds number $R_{L_\infty} = 2 \times 10^6$, the

pressure distributions in the three planes of measurement are shown in figures 24(a)-(c). Results from oil-flow visualization are added to indicate the positions of attachment and separation lines. The distribution across the semispan is typical for leading-edge separation, with a small uniform region about the centerline and a suction peak in the outboard part of the wing. The results for $M = 3$, on the contrary, do not show a suction peak, but a rather uniform pressure distribution in the outer wing region (see figs. 25(a)-(c)). As the flow visualization indicates, the height of the separated region at the higher Mach number decreases substantially and a Prandtl-Meyer expansion might occur around the leading edge and above the separated flow. The theoretical value for a Prandtl-Meyer expansion in the crossflow for $\alpha = 8°$ is pointed out in figures 25(b) and 25(c) and lies close to the measured values. If for the same Mach number the Reynolds number is increased, the basic shape of the pressure distribution does not seem to change, as seen in figures 26(a)-(c). Again, the pressure value for a Prandtl-Meyer expansion in a crossflow plane at $\alpha = 8°$ is indicated in the figures.

The skin-friction measurements at two Mach numbers and the lower Reynolds number $R_{L_\infty} = 2 \times 10^6$ were obtained with a dual-laser-beam interferometer that nonintrusively measures skin friction by monitoring the thickness change of an oil film exposed to shear stress. For a detailed description of the apparatus and technique, see reference 6. Results of the actual measurement are not yet available but will be published soon in a separate paper. However, photographs of the interference patterns which develop on the flat leeward side of the delta wing were made. Figure 27 reviews schematically the physics of reflection on thin films. Since the phase shift of the reflected beam is only a function of oil thickness, an interference pattern becomes visible at a certain thickness due to the wedge-shaped oil film. Thus, the spacing of the fringes is a direct measure for the magnitude of shear. Two photographs of "oil fringe" pattern are shown in figures 28(a) and 28(b) and compared to results from oil-flow visualization. Note that due to difficult access to the model, the leading edge of the oil film is not perpendicular to the oncoming flow; however, there is no influence on the end result. The fringe pattern in figure 28(a) for $M_\infty = 2$ and $\alpha = 8°$ displays three shear peaks in the outer part of the wing. These are attributed to the high shear level at attachment lines, although the agreement with oil-flow results discussed earlier is not good. However, it is believed that the oil-fringe pattern gives better resolution since the oil film is within the sublayer. For $M_\infty = 3$ and $\alpha = 8°$, the agreement between oil-fringe pattern and oil-flow visualization is rather good, as seen in figure 28(b). The second peak outboard of the maximum shear region might be associated with the large-scale streamwise vortices as seen in figure 14. In both cases (see figs. 28(a) and 28(b)), the centerline region exhibits traces of streamwise vortices.

CONCLUSIONS

An experimental investigation of the supersonic flow about a 70° swept delta wing was carried out. Static pressure distributions, flow visualization,

and shear-stress measurements were made at two Mach numbers, two Reynolds numbers, and various angles of attack. The essential results are the following:

1. Test results were obtained for two types of flow, leading-edge separation and separation with shock; the latter is strongly Reynolds number dependent.

2. Unexpected strong streamwise vortices develop and influence a great part of the flow field. These longitudinal vortices were not only observed in the attached flow region about the meridian plane, but also in the cross-flow in the outboard part of the wing.

3. A fast and easy indication for shear-stress distribution is given by photographs of laser generated oil-fringe patterns which develop when a thin oil film is placed on the model surface.

Together with laser-Doppler-velocimeter measurements for all three velocity components, these results will allow deeper insight into the physics, discussed herein, of leeward flow over delta wings and provide excellent data for comparison with computation.

REFERENCES

1. Szodruch, J. G.; and Peake, D. J.: Leeward Flow Over Delta Wings at Supersonic Speeds. NASA TM-81187, April 1980.

2. Maltby, R. L.: Flow Visualization in Wind Tunnels Using Indicators. AGARDograph 70, April 1962.

3. Ginoux, J. J.: Instabilité de la Couche Limite sur Ailes en Flèche (Instability of the Boundary Layer on Swept Wings). Zeitschr. für Flugwissenschaften, 15 Jahrgang, Heft 8/9, 1967, pp. 302-305.

4. McDevitt, J. B.; and Mellenthin, J. A.: Upwash Pattern on Ablating and Non-ablating Cones at Hypersonic Speeds. NASA TN D-5346, July 1969.

5. Vigneron, Y. C.; Rakich, J. V.; and Tannehill, J. C.: Calculation of Supersonic Viscous Flow Over Delta Wings with Sharp Subsonic Leading Edges. AIAA Paper 78-1137, July 1978.

6. Monson, D. J.; and Higuchi, H.: Skin Friction Measurements by a New Nonintrusive Double-Laser-Beam Oil Viscosity Balance Technique. AIAA Paper 80-B73, July 1980.

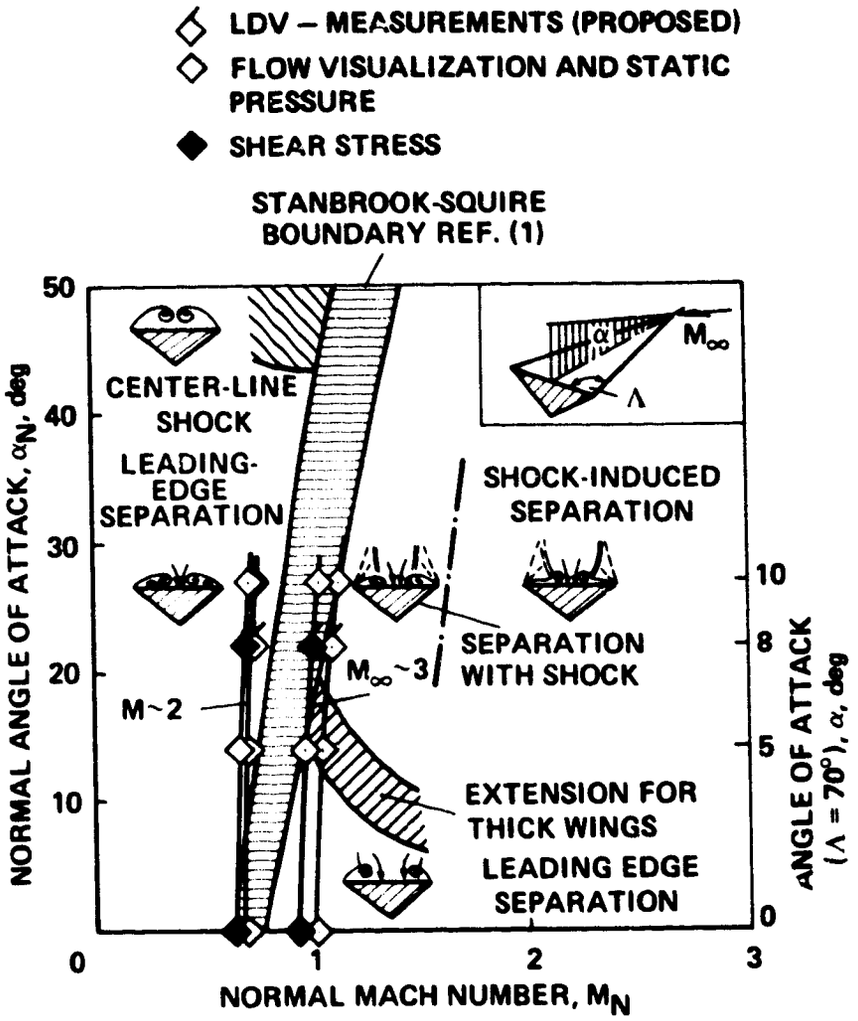

Figure 1.- Trajectory of experimental flow conditions in α_N vs M_N diagram.

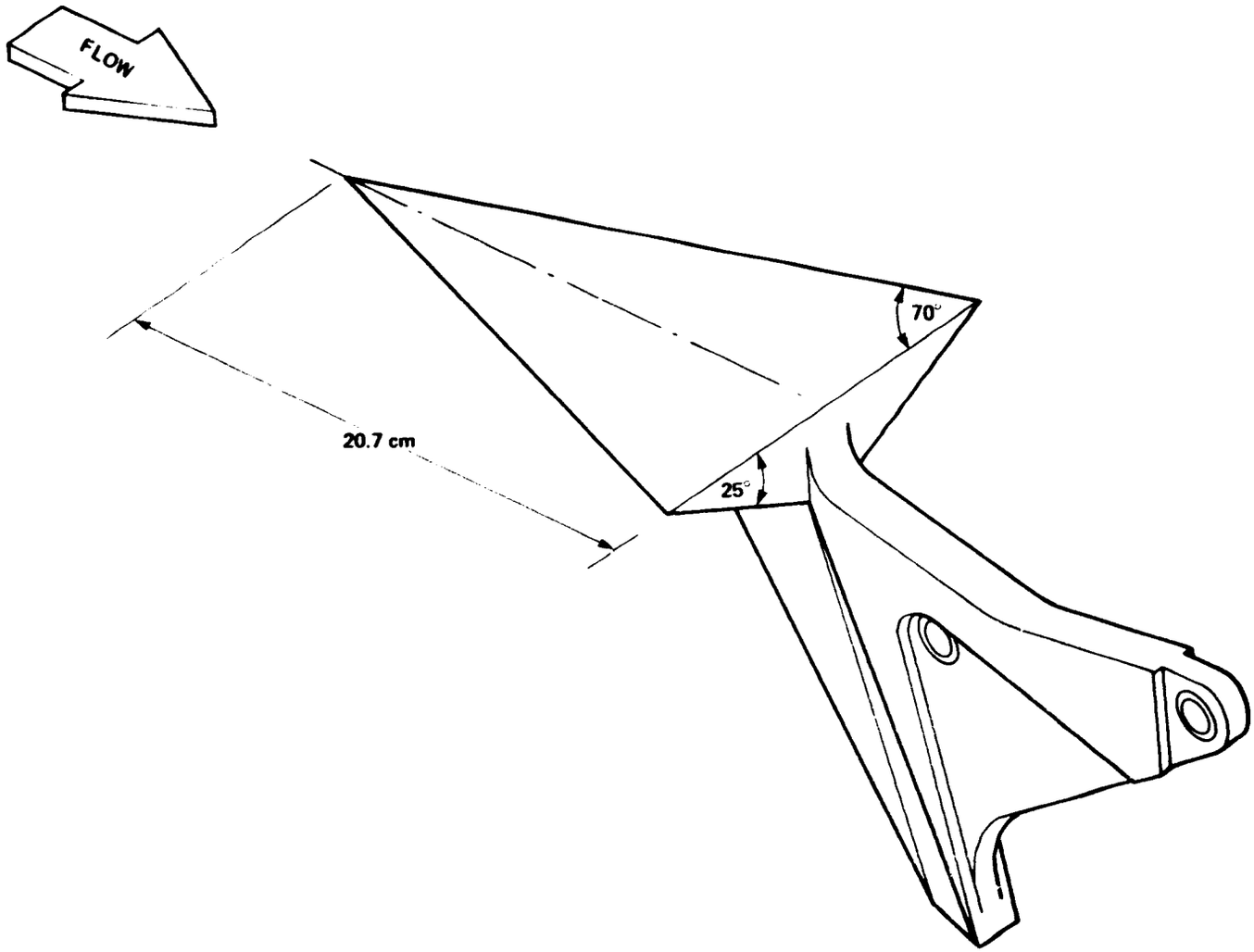

Figure 2.- Delta wing with strut support.

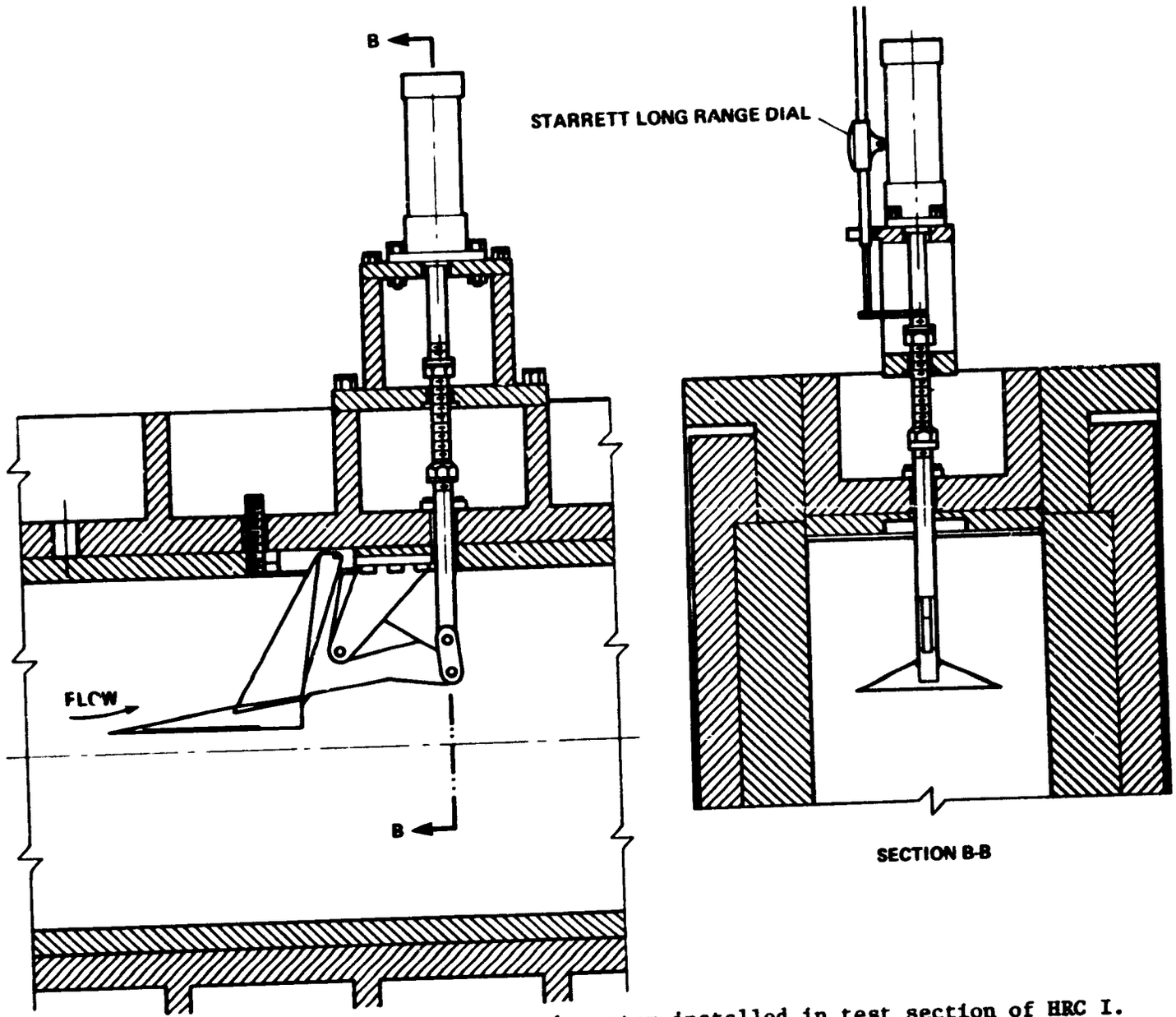

Figure 3.- Model and angle of attack system installed in test section of HRC I.

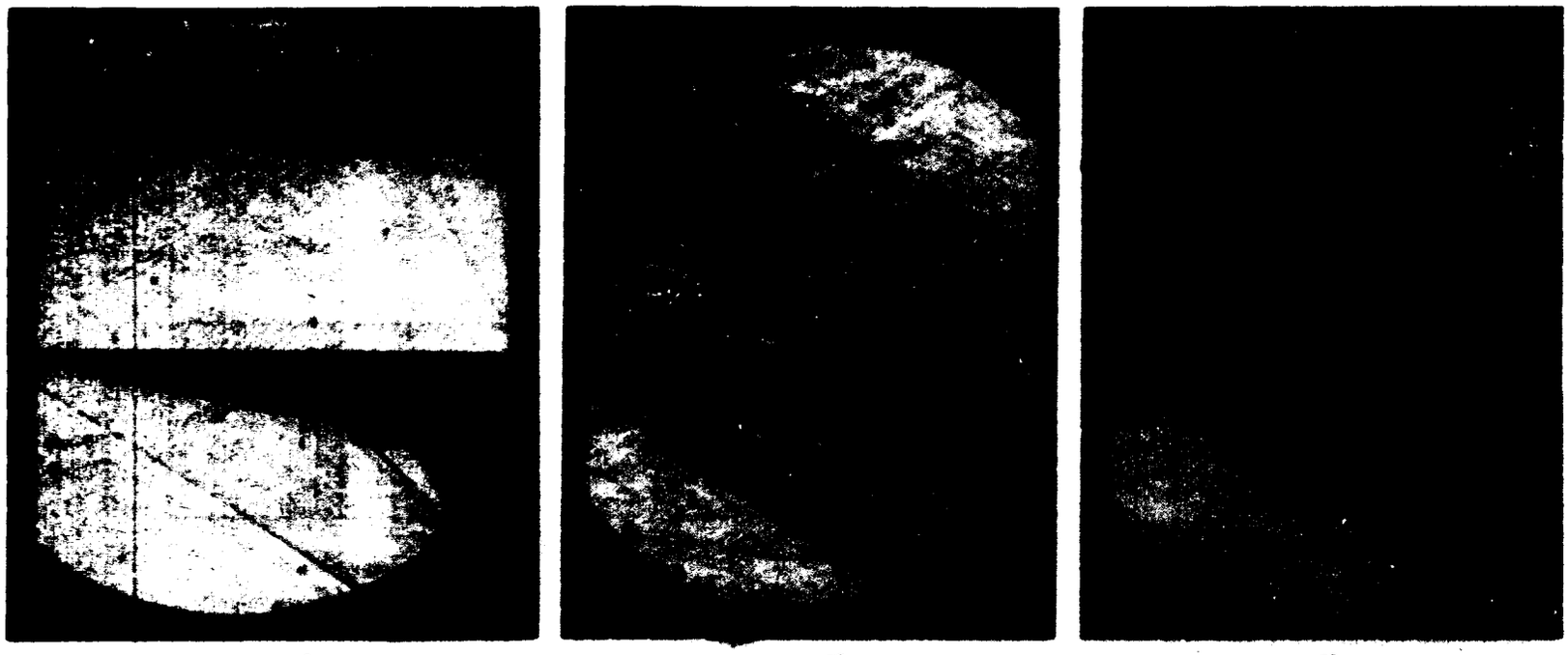

(a) $R_{L_\infty} = 2 \times 10^6$.

Figure 4.- Schlieren pictures of delta wing at angle of attack, $M_\infty = 2$.

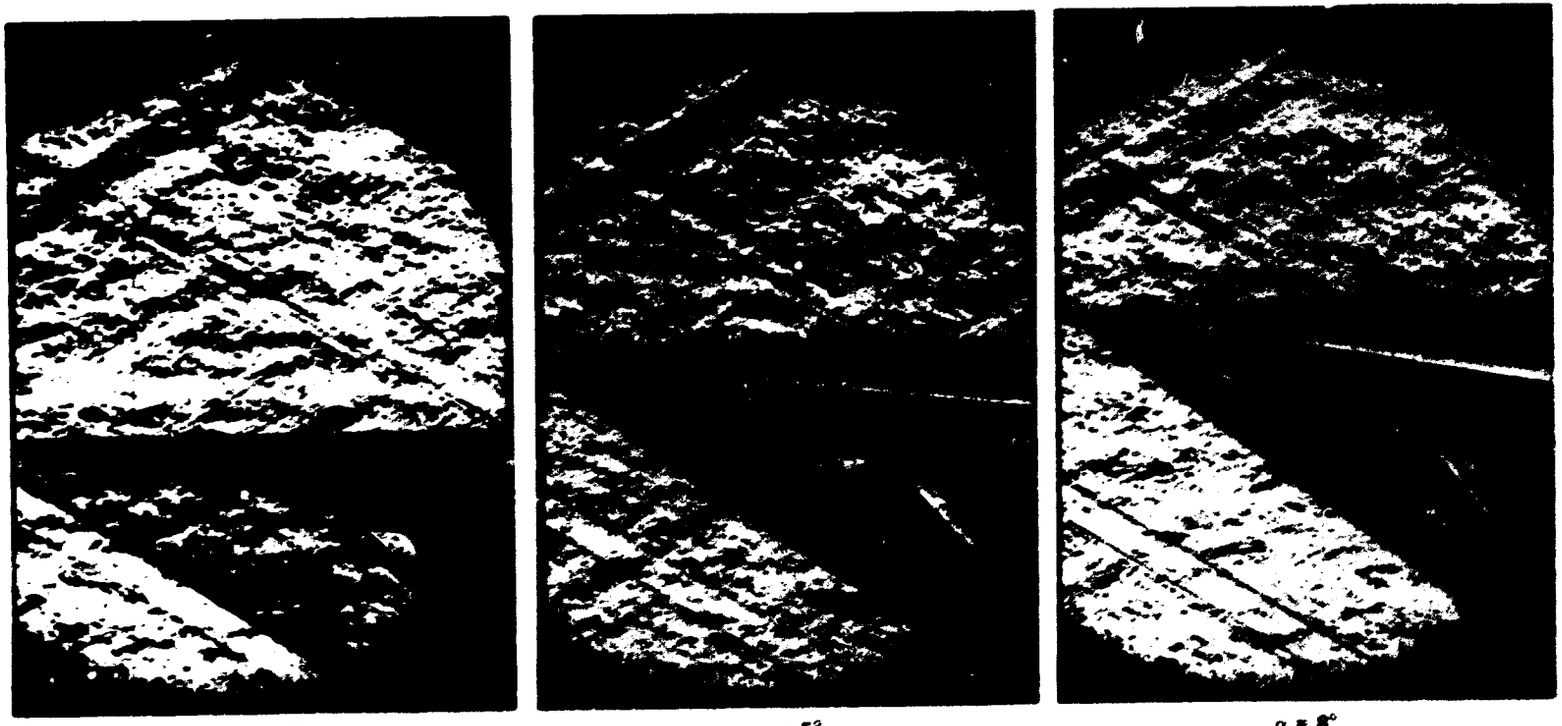

(b) $R_{L_\infty} = 25 \times 10^6$.

Figure 4.- Concluded.

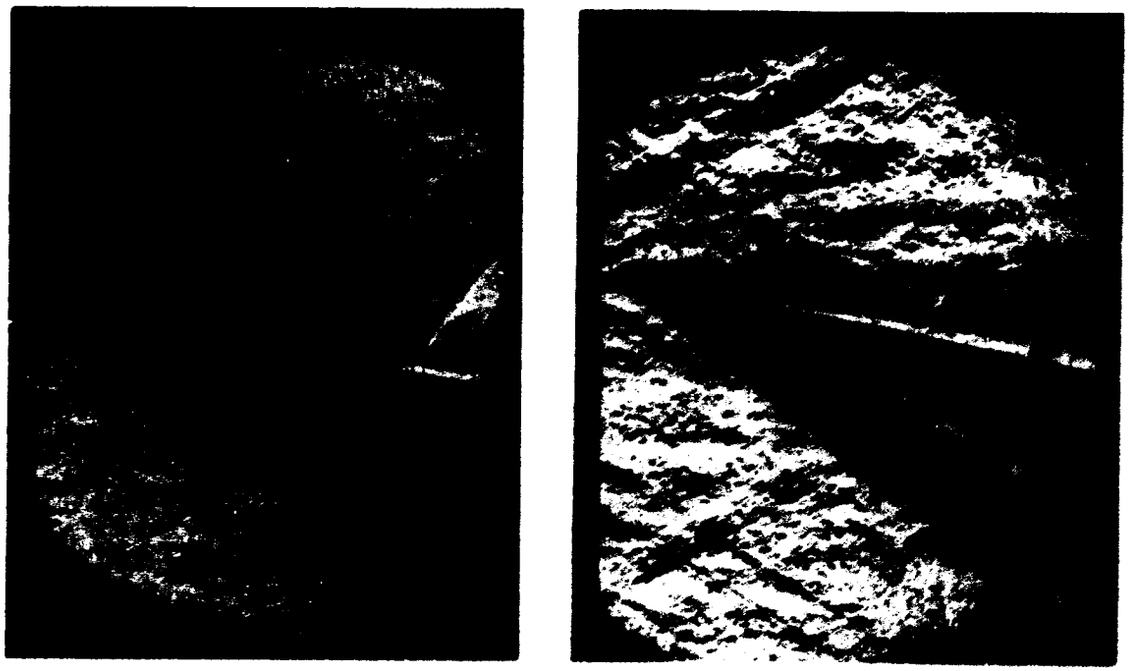

Figure 5.- Strut interference on leeward side induced by detached shock wave; $M_\infty = 2$, $\alpha = 10°$.

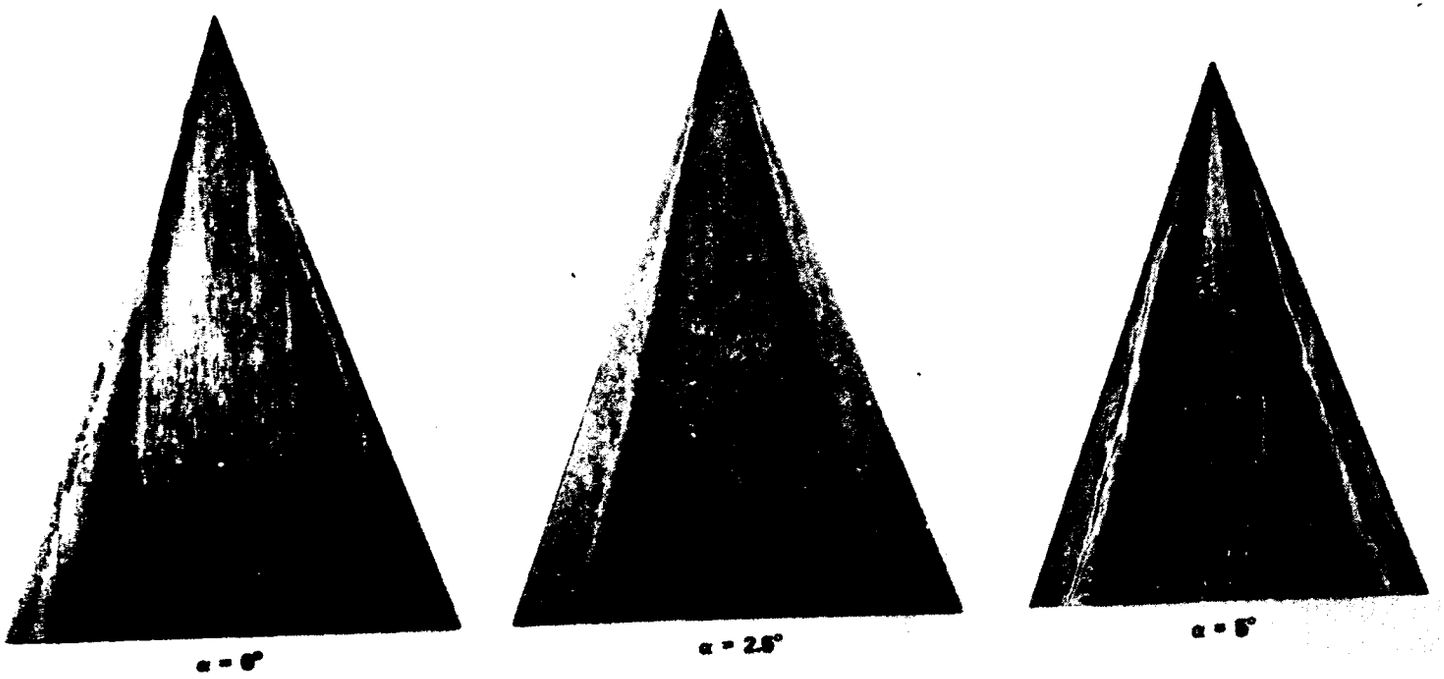

Figure 6.- Oil-flow visualization over the leeward side of the delta wing at $M_\infty = 2$, $R_{L_\infty} = 2 \times 10^6$ and various angles of attack.

Figure 6.- Concluded.

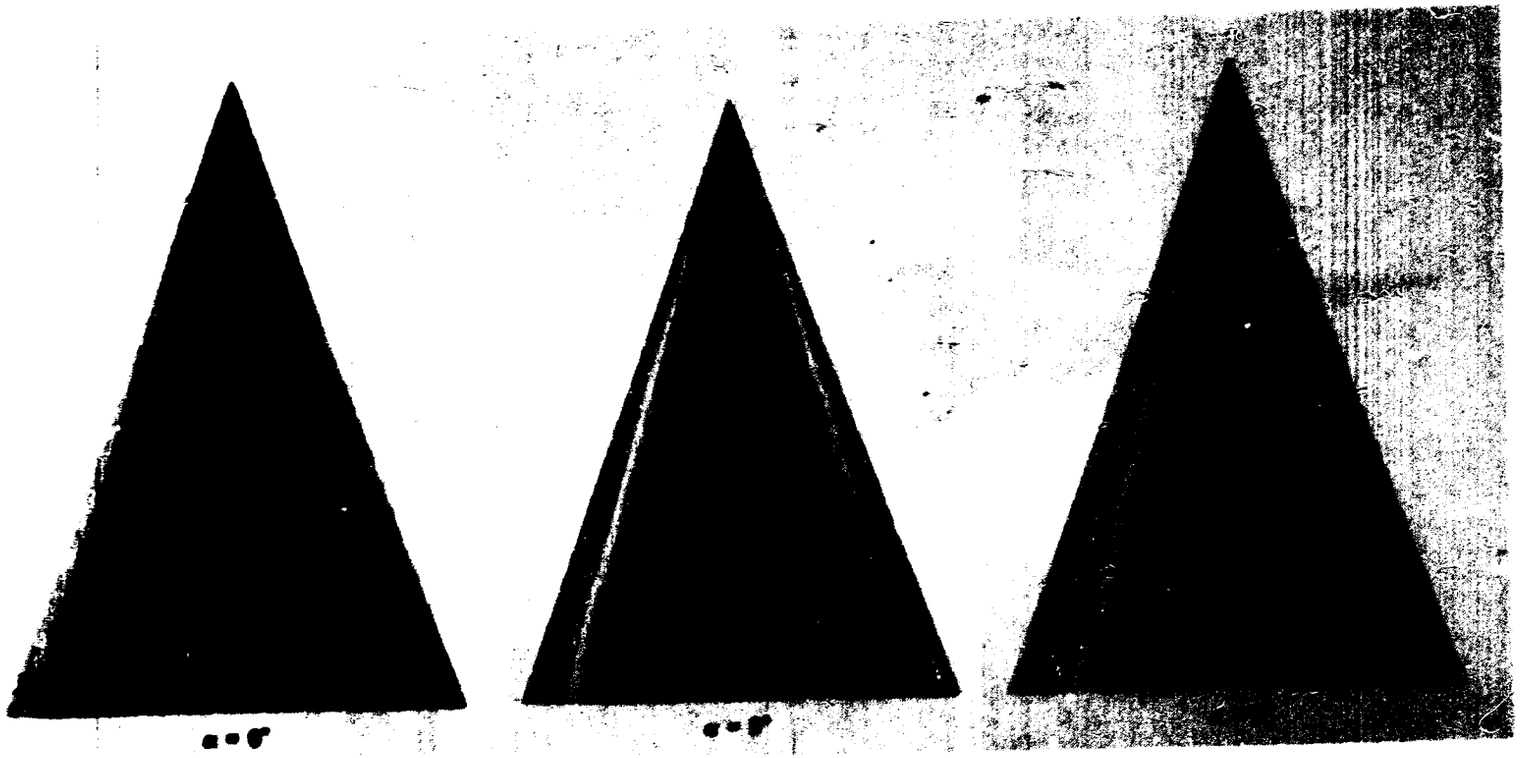

Figure 7.- Oil-flow visualization over the leeward side of the delta wing at $M_\infty = 2$, $R_{L_\infty} = 25 \times 10^6$ and various angles of attack.

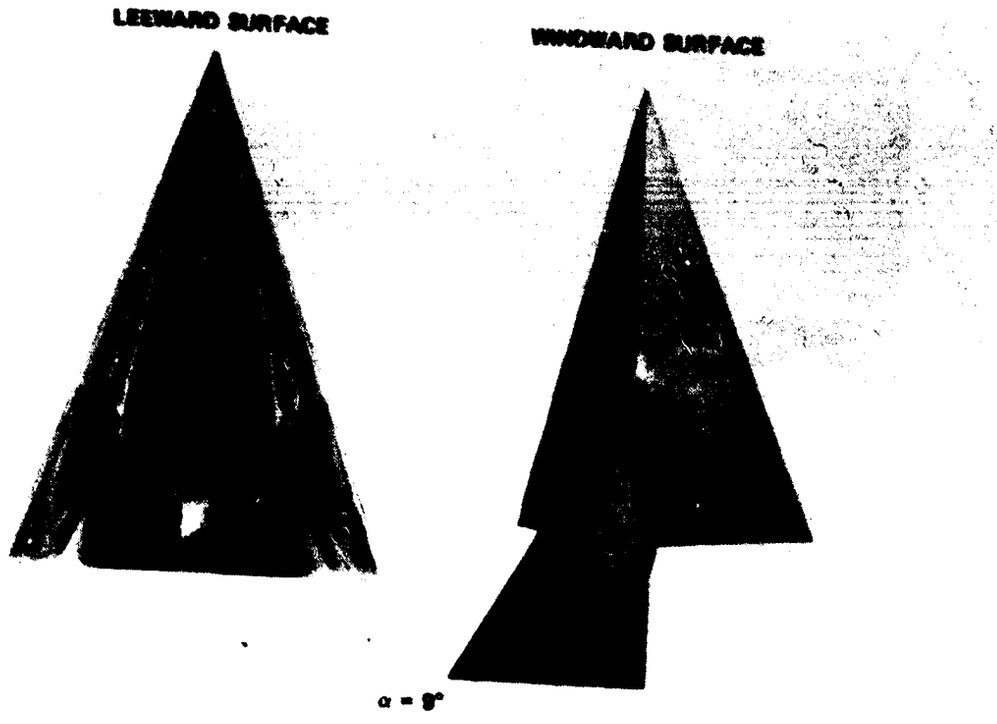

Figure 8.- Oil-flow visualization over the upper and lower sides of the delta wing at $M_\infty = 2$, $R_{L_\infty} = 25 \times 10^6$ and $\alpha = 9°$.

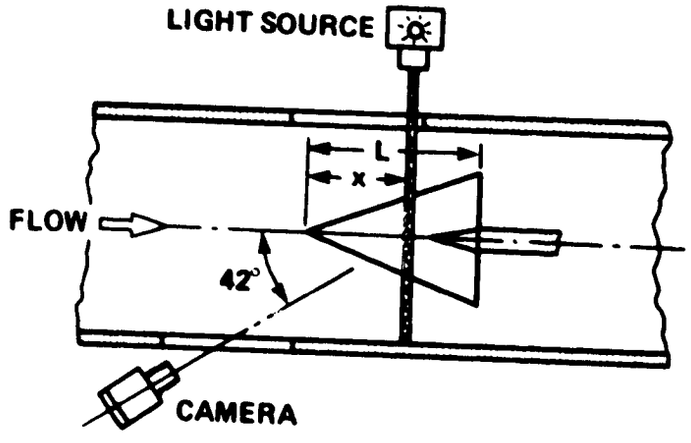

Figure 9.- Test arrangement for vapor screen visualization.

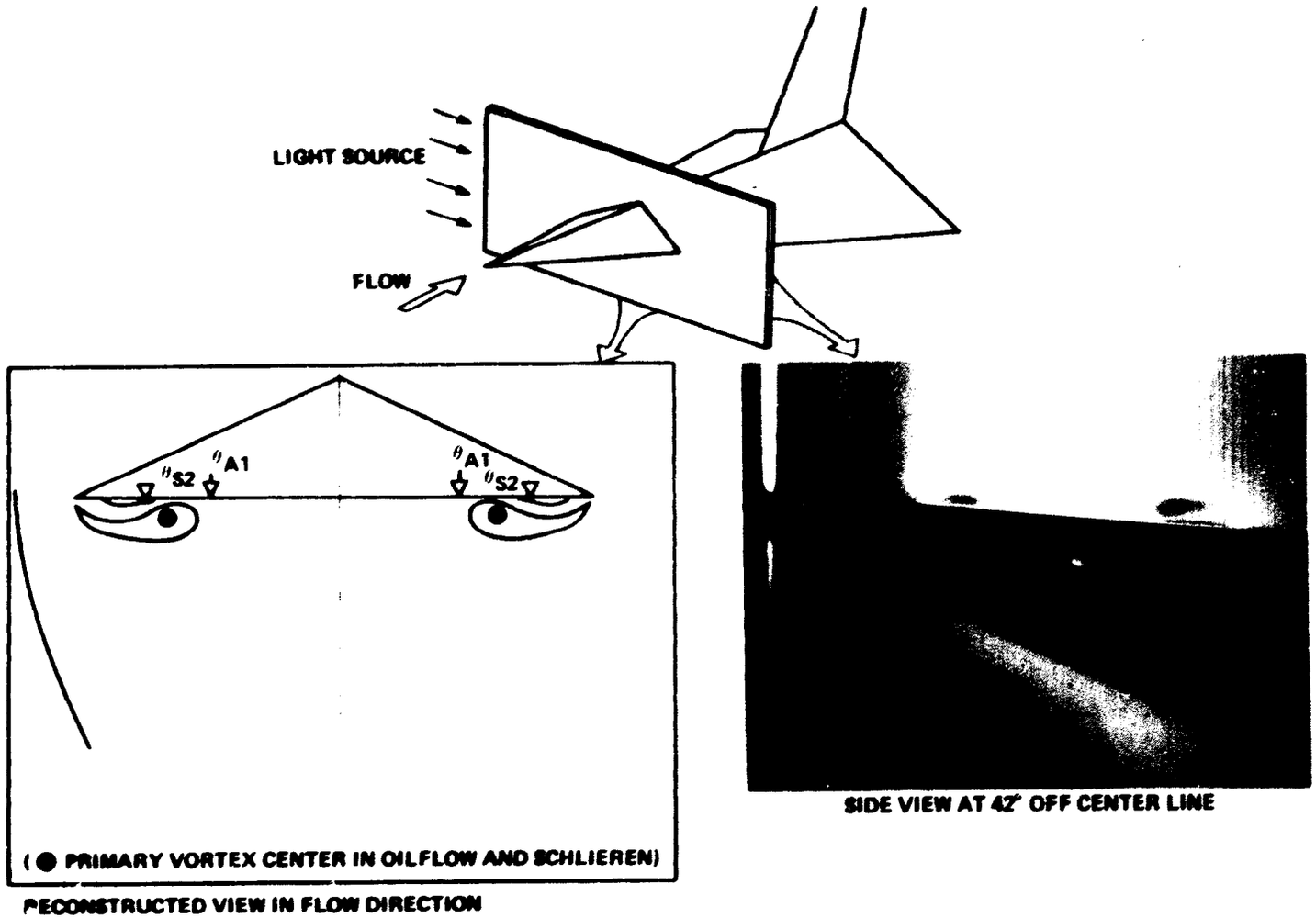

(a) $\alpha = 5°$.

Figure 10.- Vapor screen at $M_\infty = 2$, $R_{L_\infty} = 2 \times 10^6$.

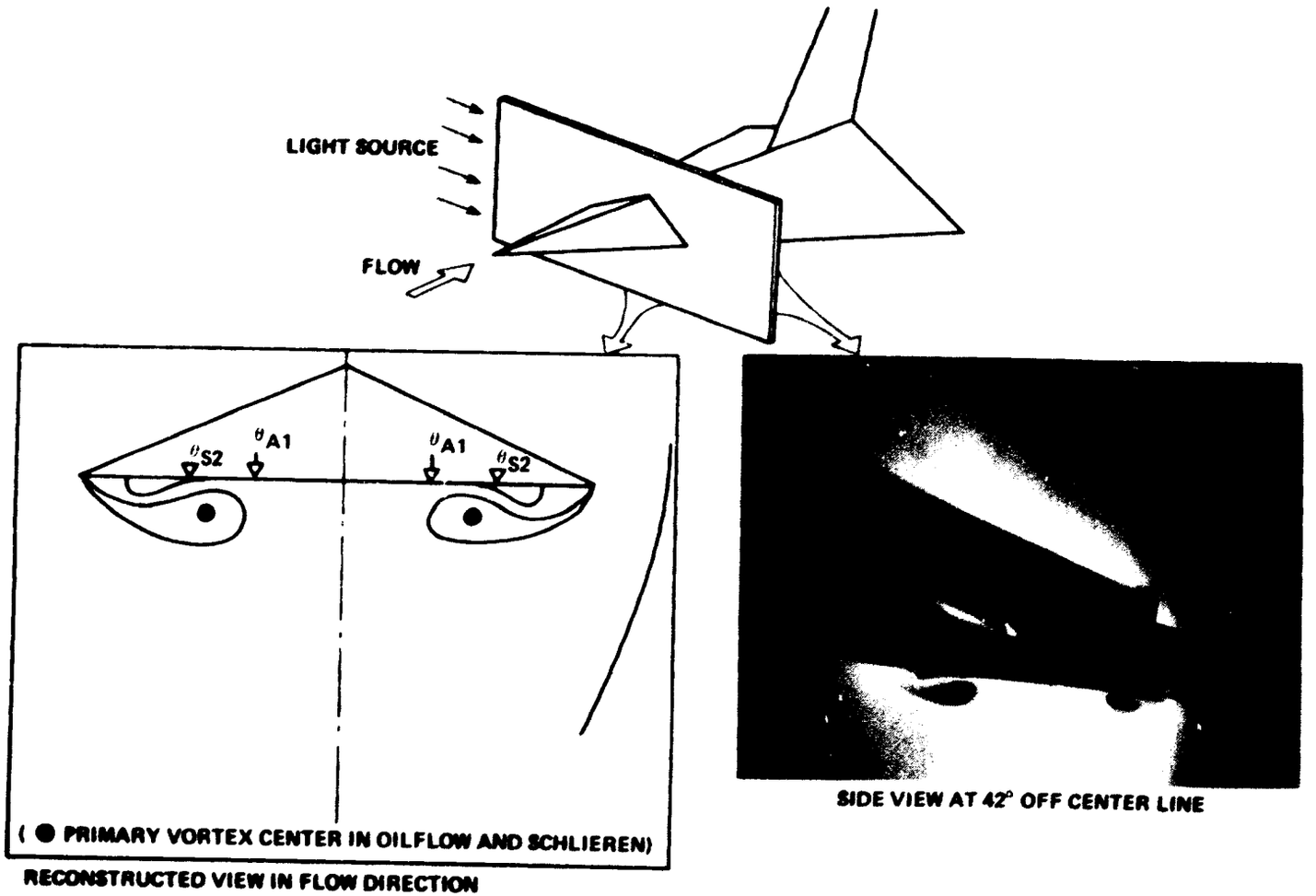

(b) $\alpha = 8°$.

Figure 10.- Concluded.

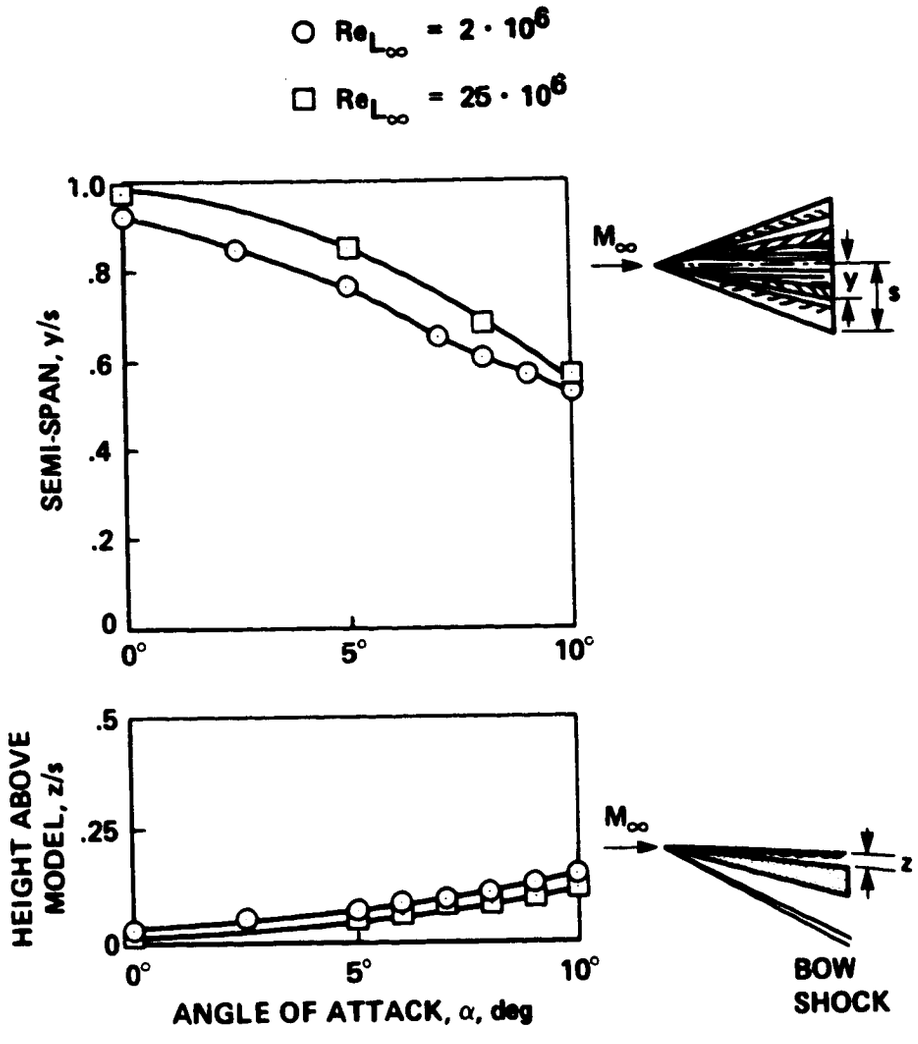

Figure 11.- Secondary separation line and position of primary vortex above delta wing, M_∞ = 2.0. Test 41.

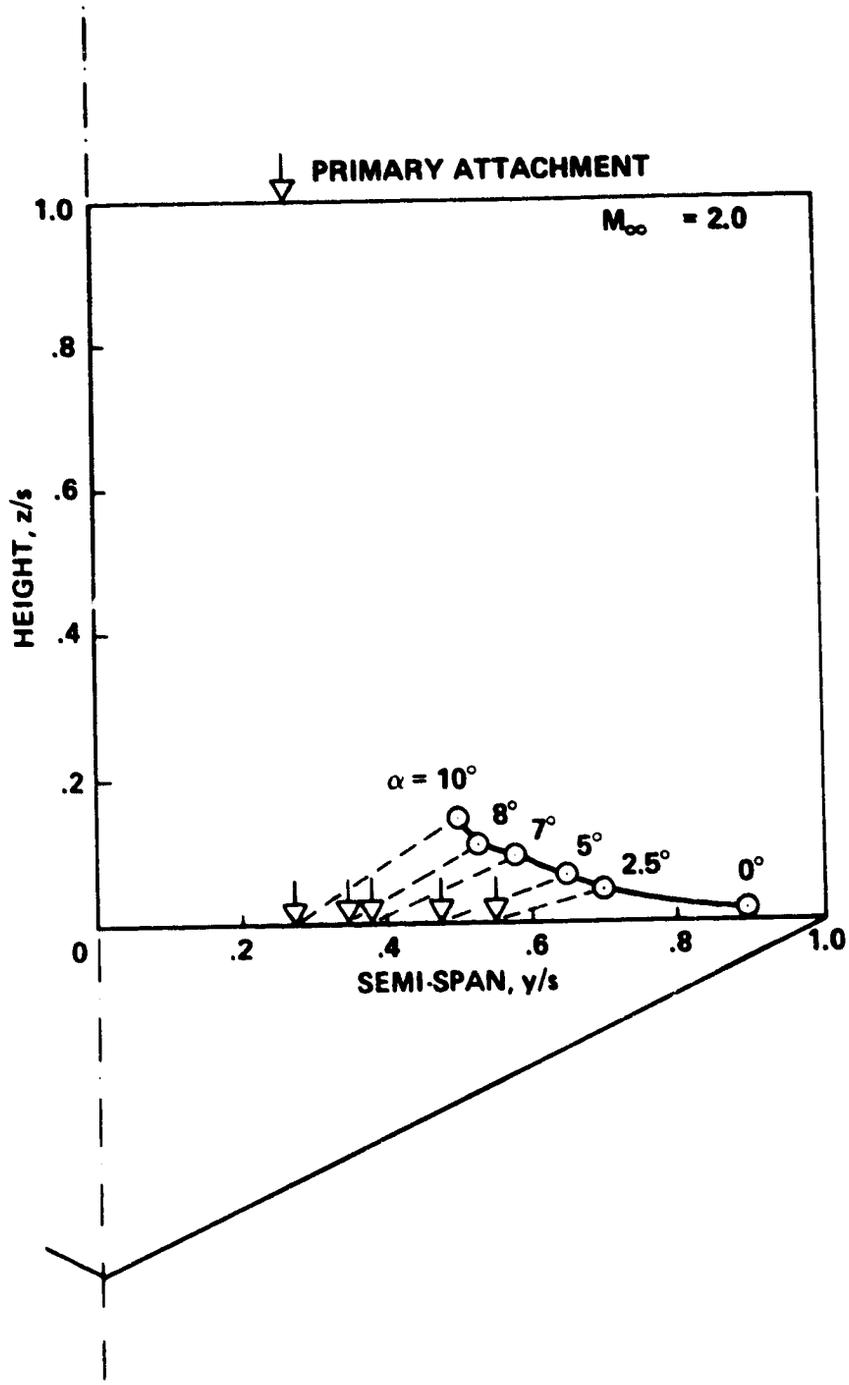

(a) $R_{L_\infty} = 2 \times 10^6$.

Figure 12.- Primary vortex position above leeward side of delta wing.

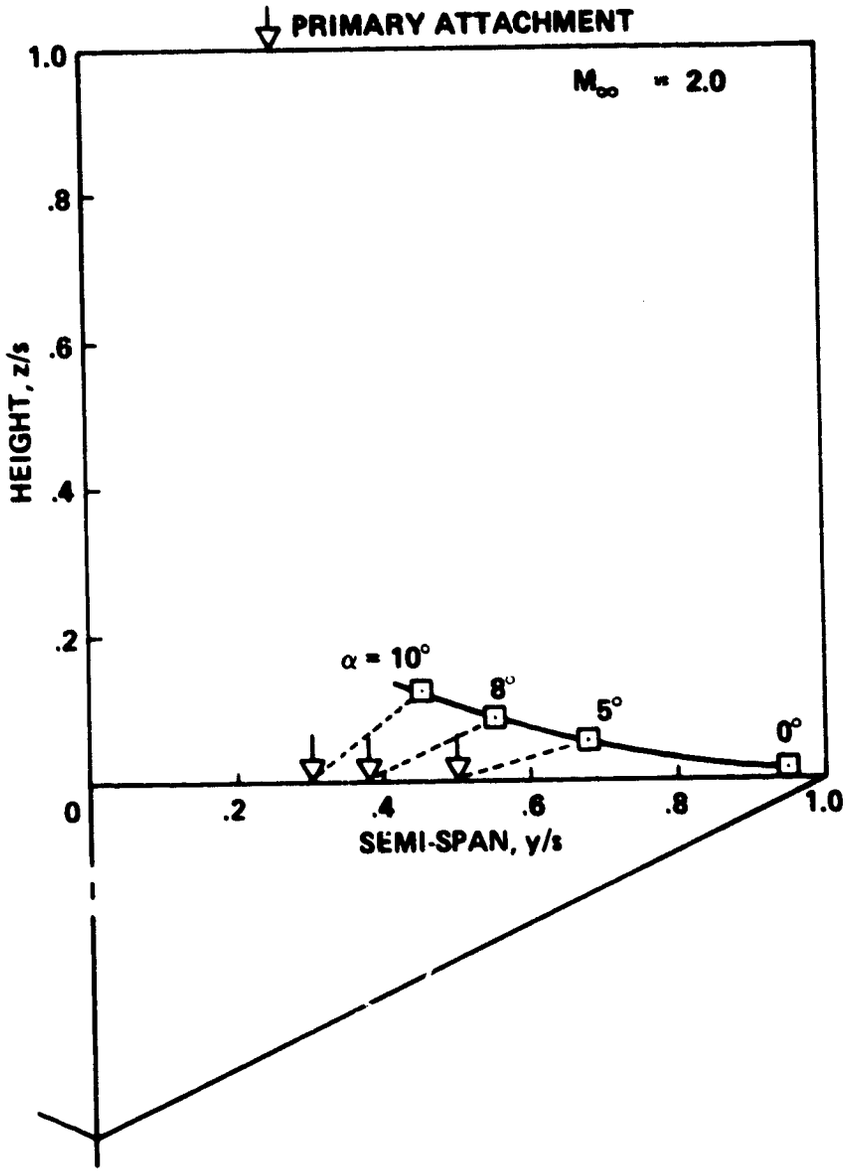

(b) $R_{L_\infty} = 25 \times 10^6$.

Figure 12.- Concluded.

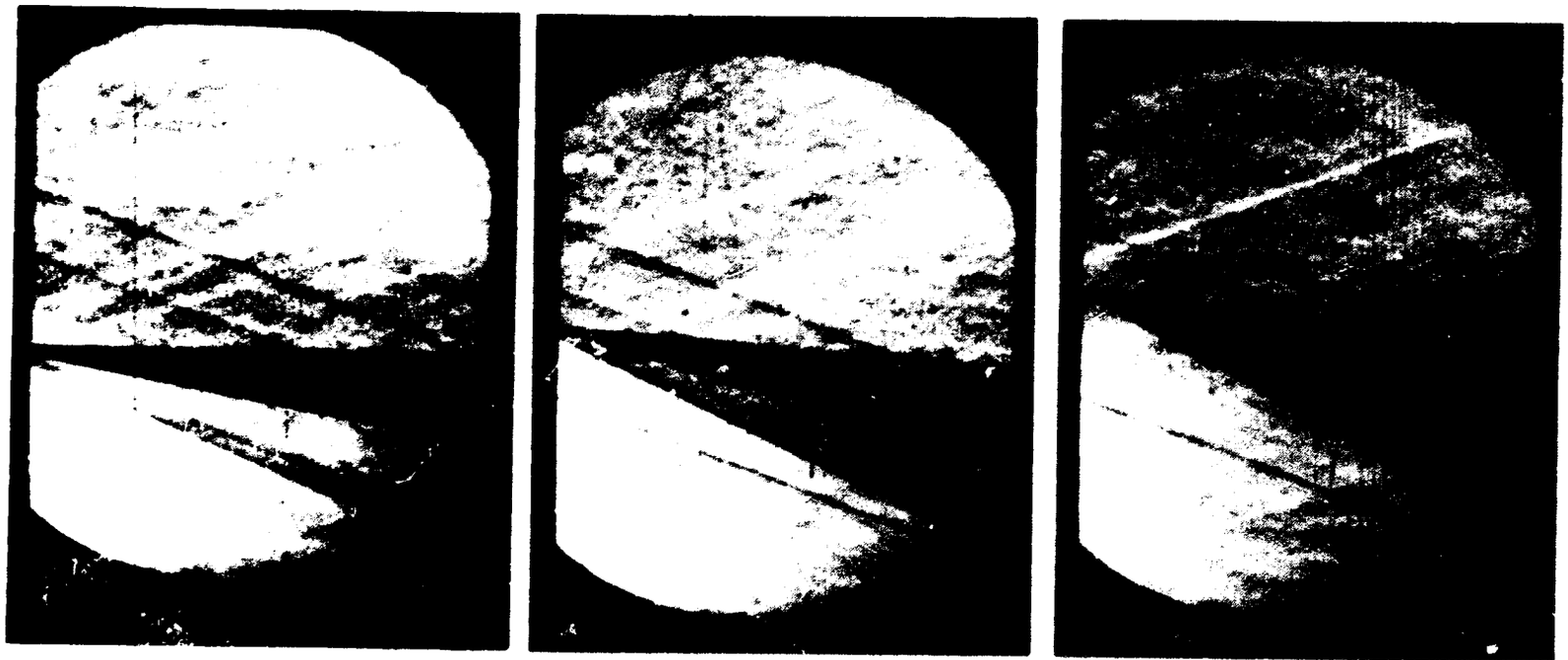

(a) $R_{L_\infty} = 2 \times 10^6$.

Figure 13.- Schlieren pictures of delta wing at angle of attack, $M_\infty = 3$.

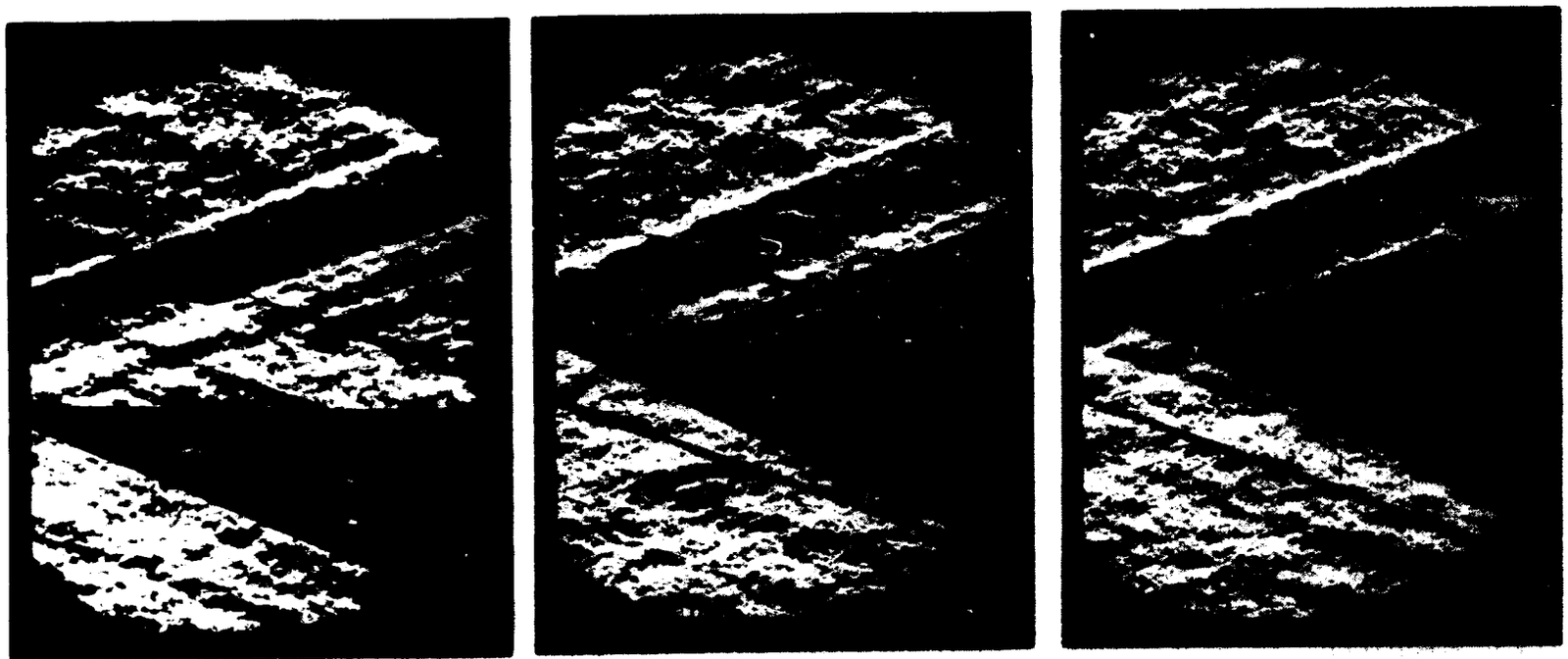

(b) $R_{L_\infty} = 25 \times 10^6$.

Figure 13.- Concluded.

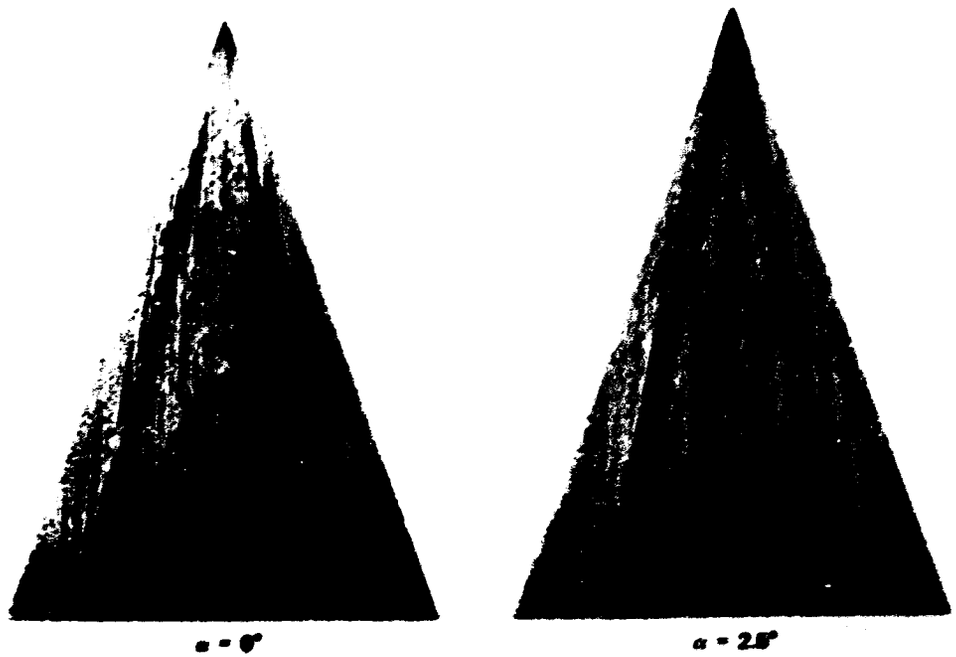

(a) (b)

Figure 14.- Oil-flow visualization on the leeward side of the delta wing at $M_\infty = 3$, $R_{L_\infty} = 2 \times 10^6$.

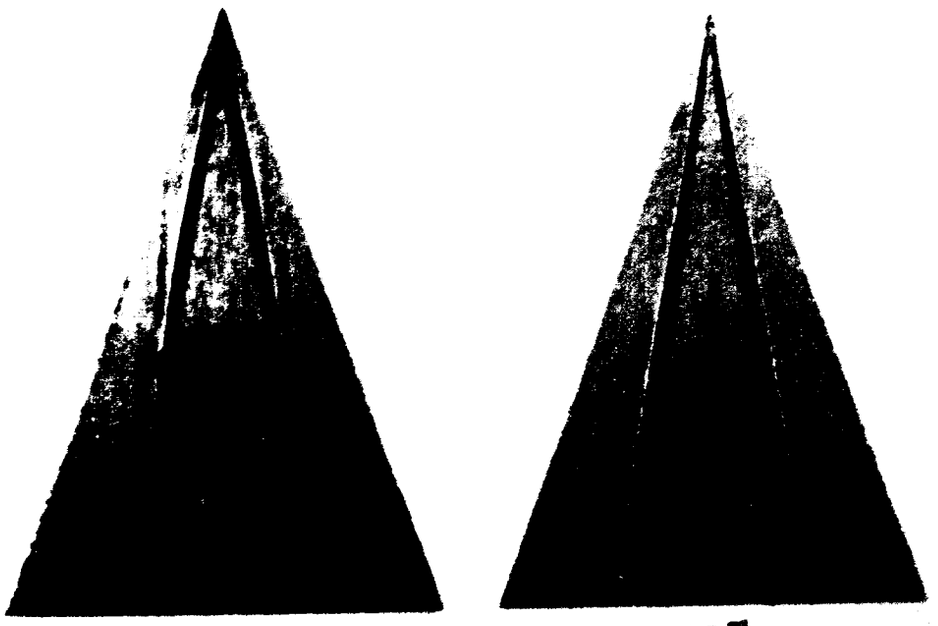

(c) (d)

Figure 14.- Continued.

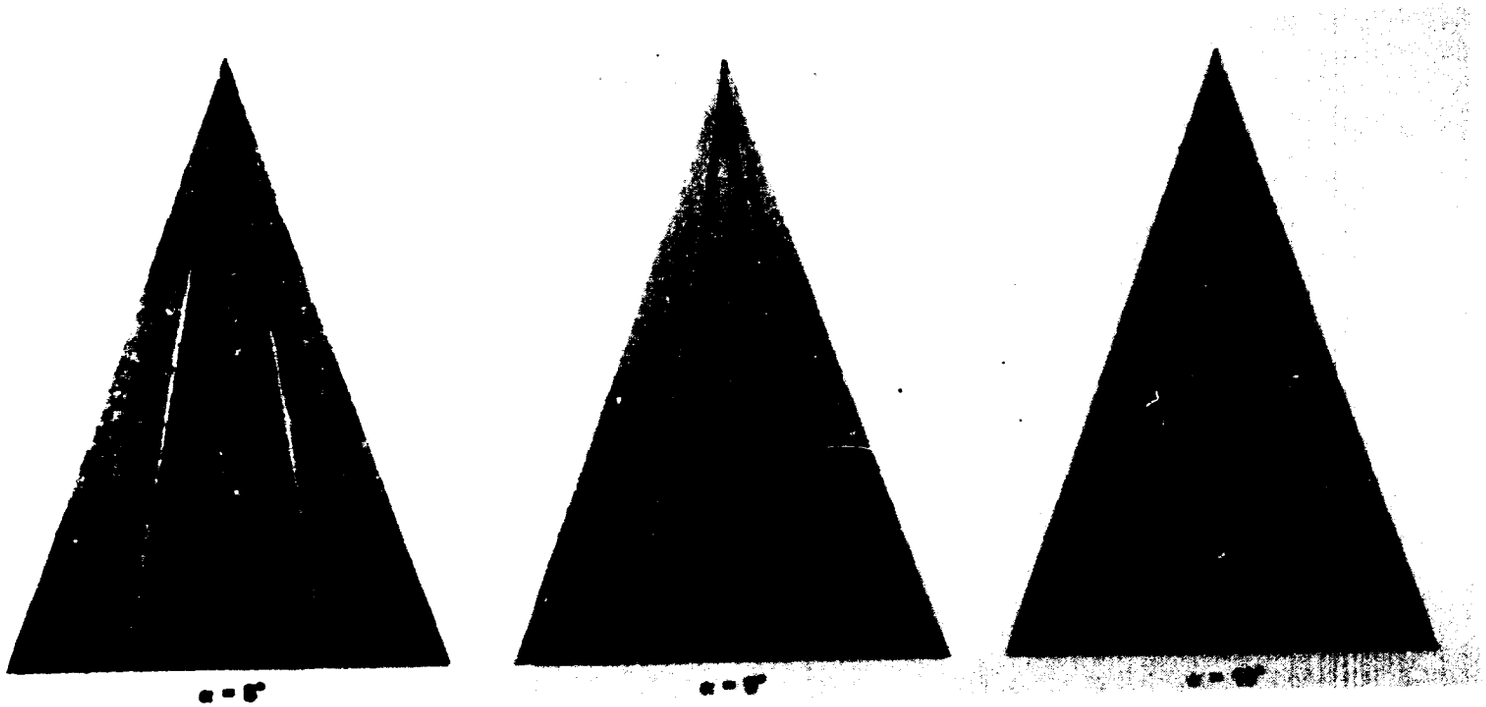

(e) (f) (g)

Figure 14.- Concluded.

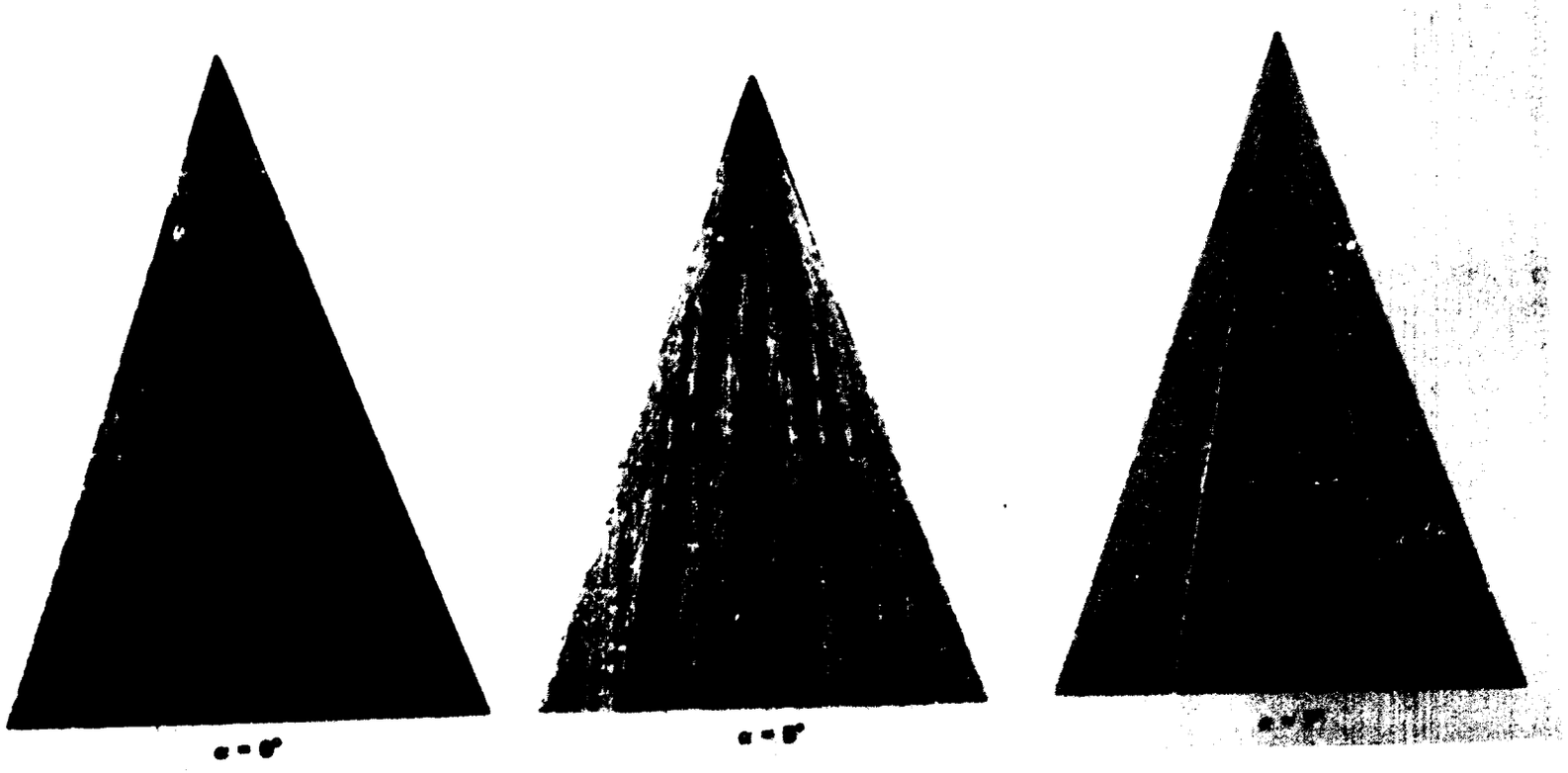

(a) (b) (c)

Figure 15.- Oil-flow visualization of the tip region on the leeward side of the delta wing at $M_\infty = 3$, $R_{L_\infty} = 2 \times 10^6$.

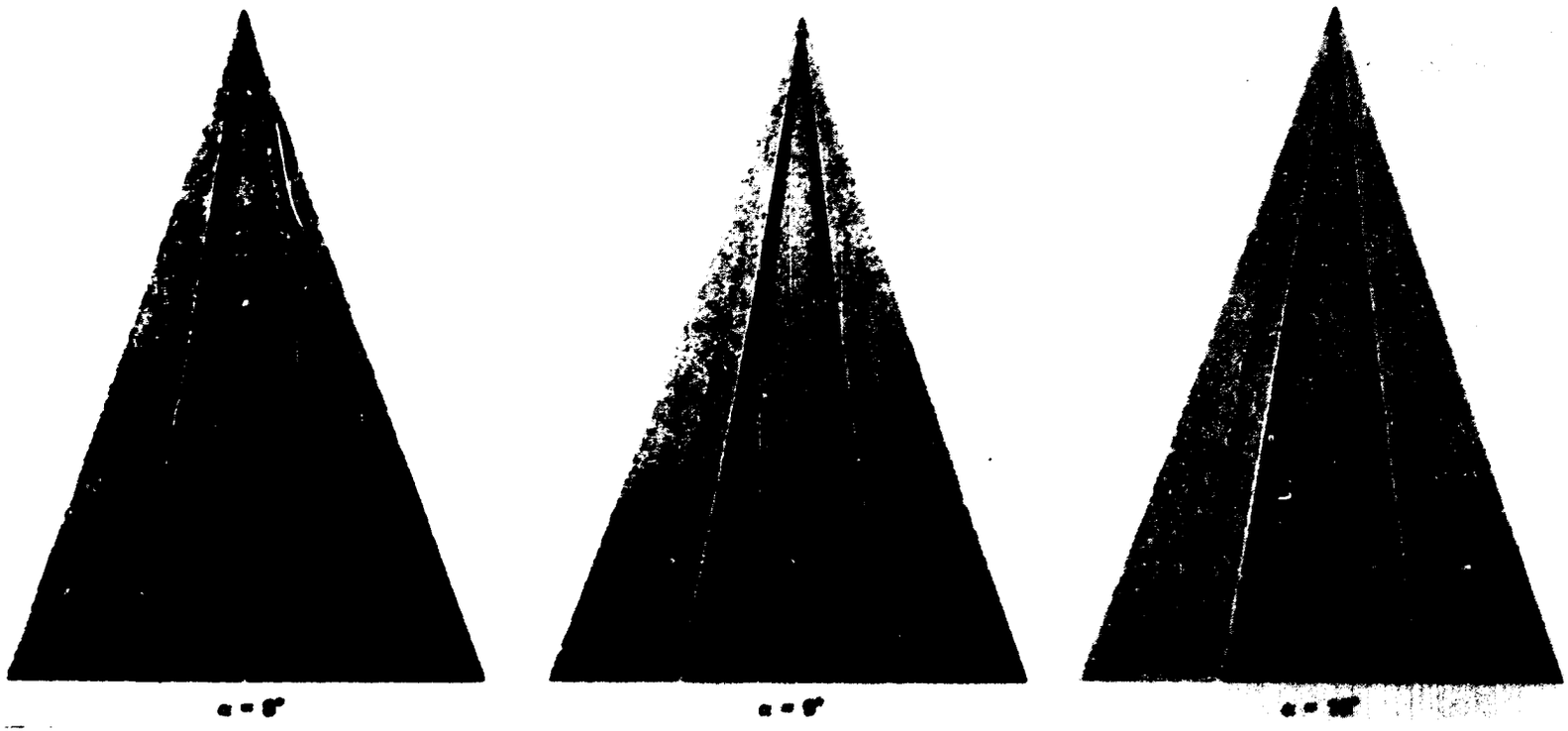

(d) (e) (f)

Figure 15.- Concluded.

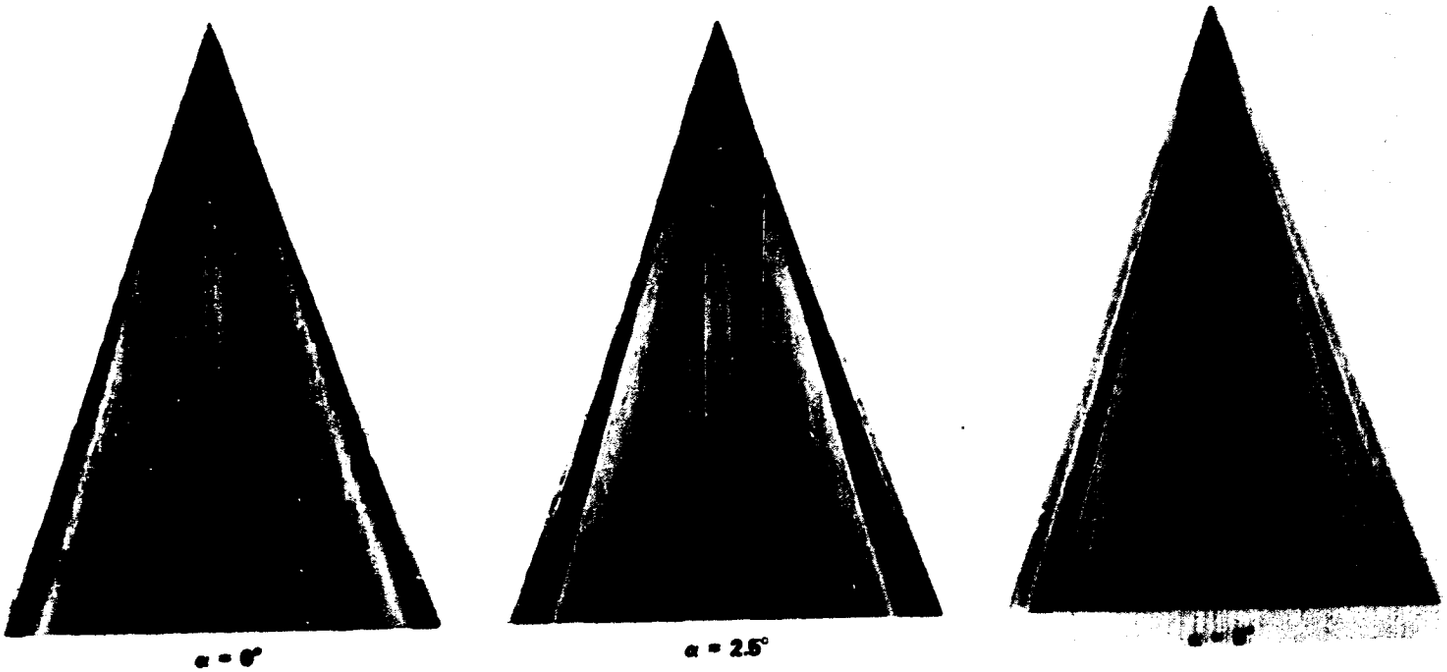

Figure 16.- Oil-flow visualization on the leeward side of the delta wing at $M_\infty = 3$, $R_{L_\infty} = 25 \times 10^6$

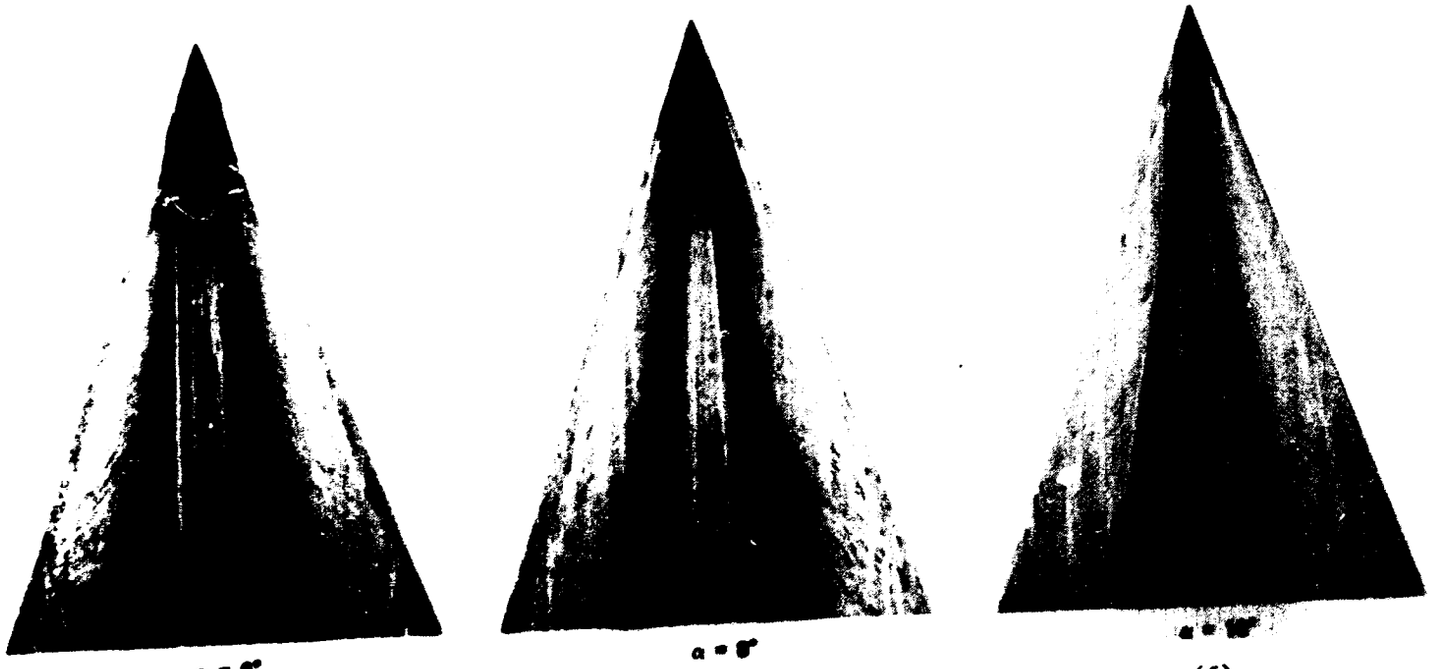

(d) (e) (f)

Figure 16.- Concluded.

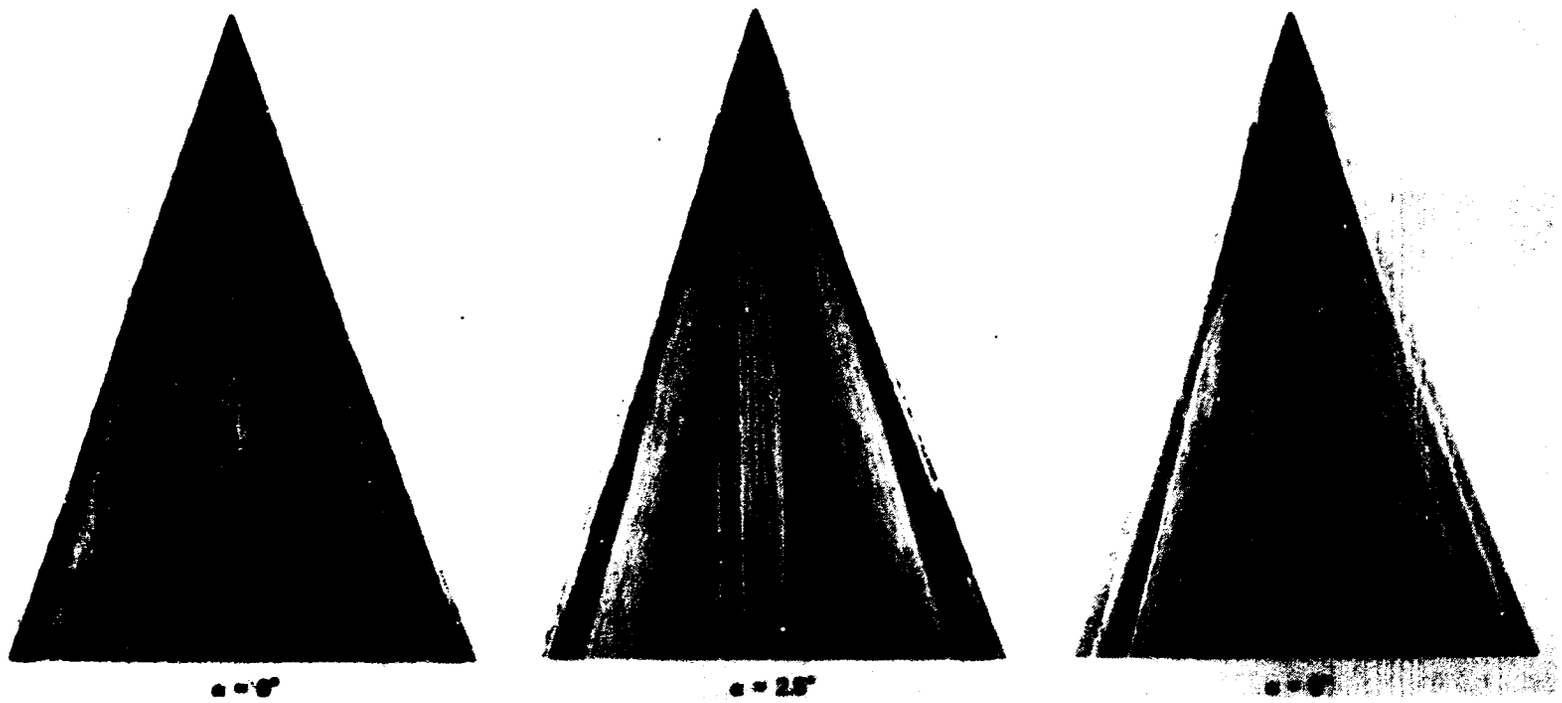

(a) (b) (c)

Figure 17.- Oil-flow visualization of the tip region on the leeward side of the delta wing at $M_\infty = 3$, $R_{L_\infty} = 25 \times 10^6$.

(d)

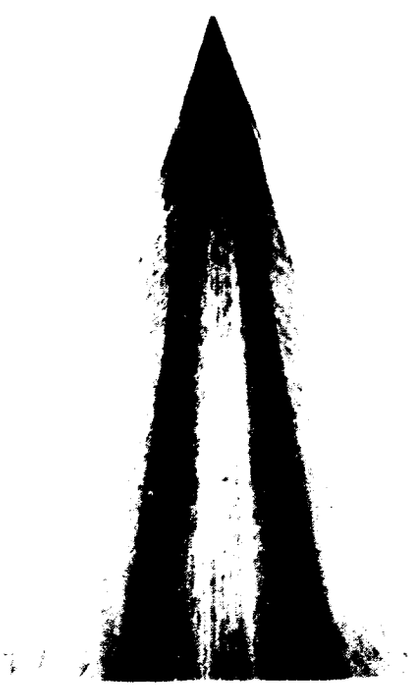

(e)

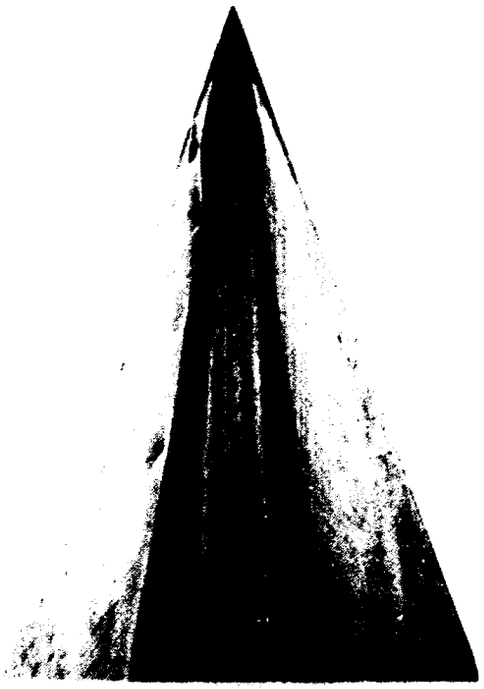

(f)

Figure 17.- Concluded.

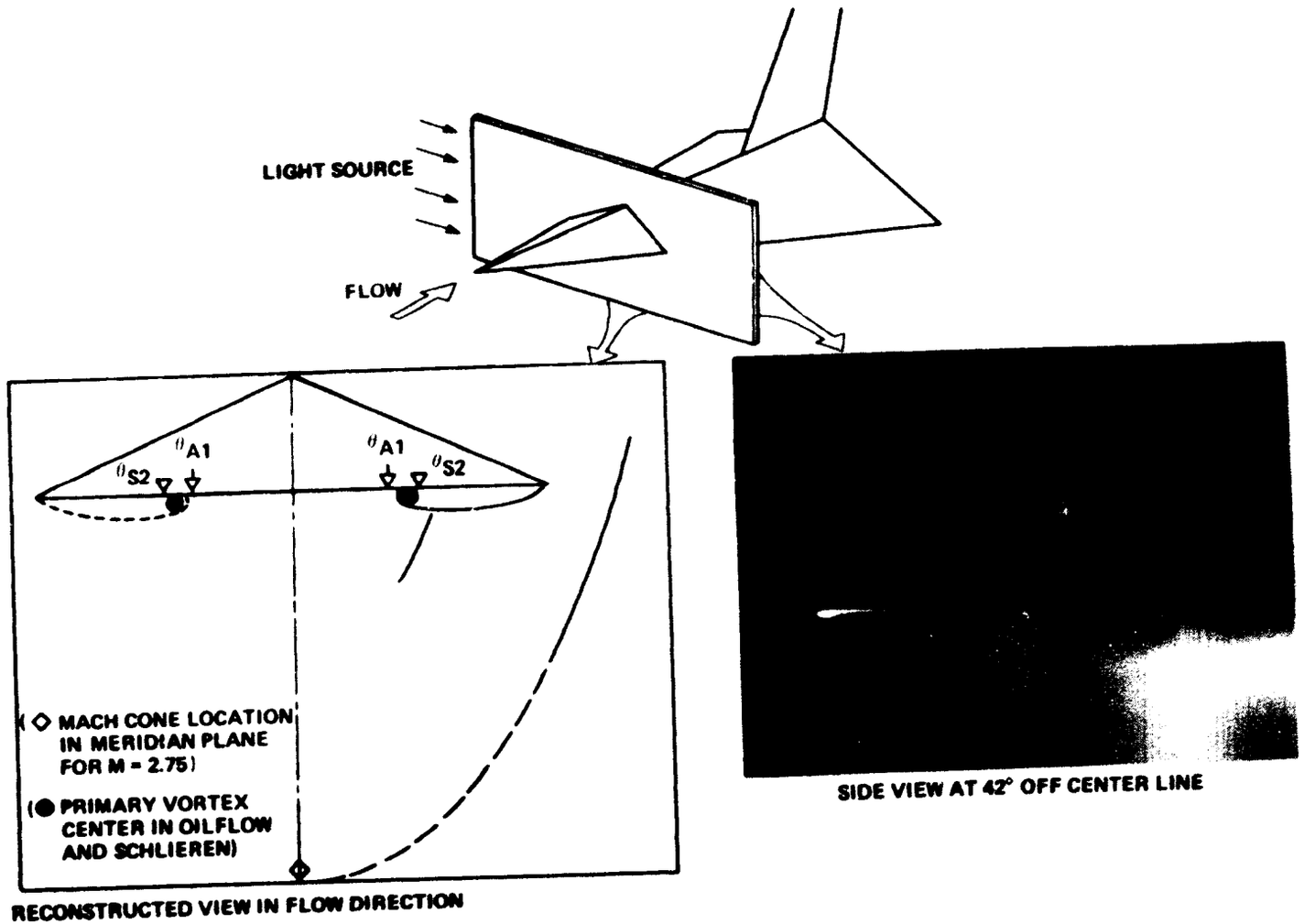

(a) $\alpha = 5°$, $R_{L_\infty} = 2 \times 10^6$.

Figure 18.- Vapor screen at $M_\infty = 3$, $x/L = 0.68$.

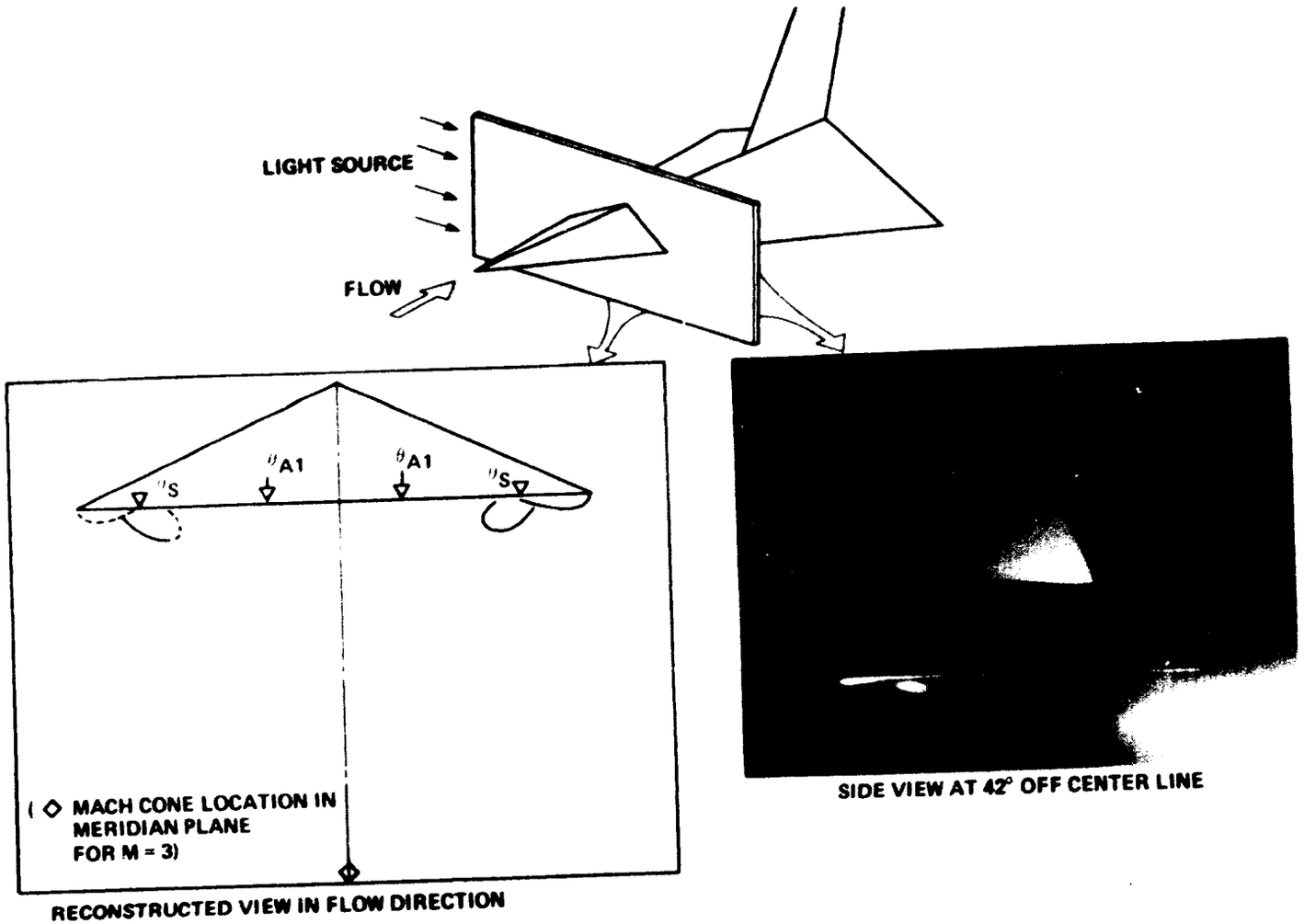

(b) $\alpha = 5°$, $R_{L_\infty} = 25 \times 10^6$.

Figure 18.- Continued.

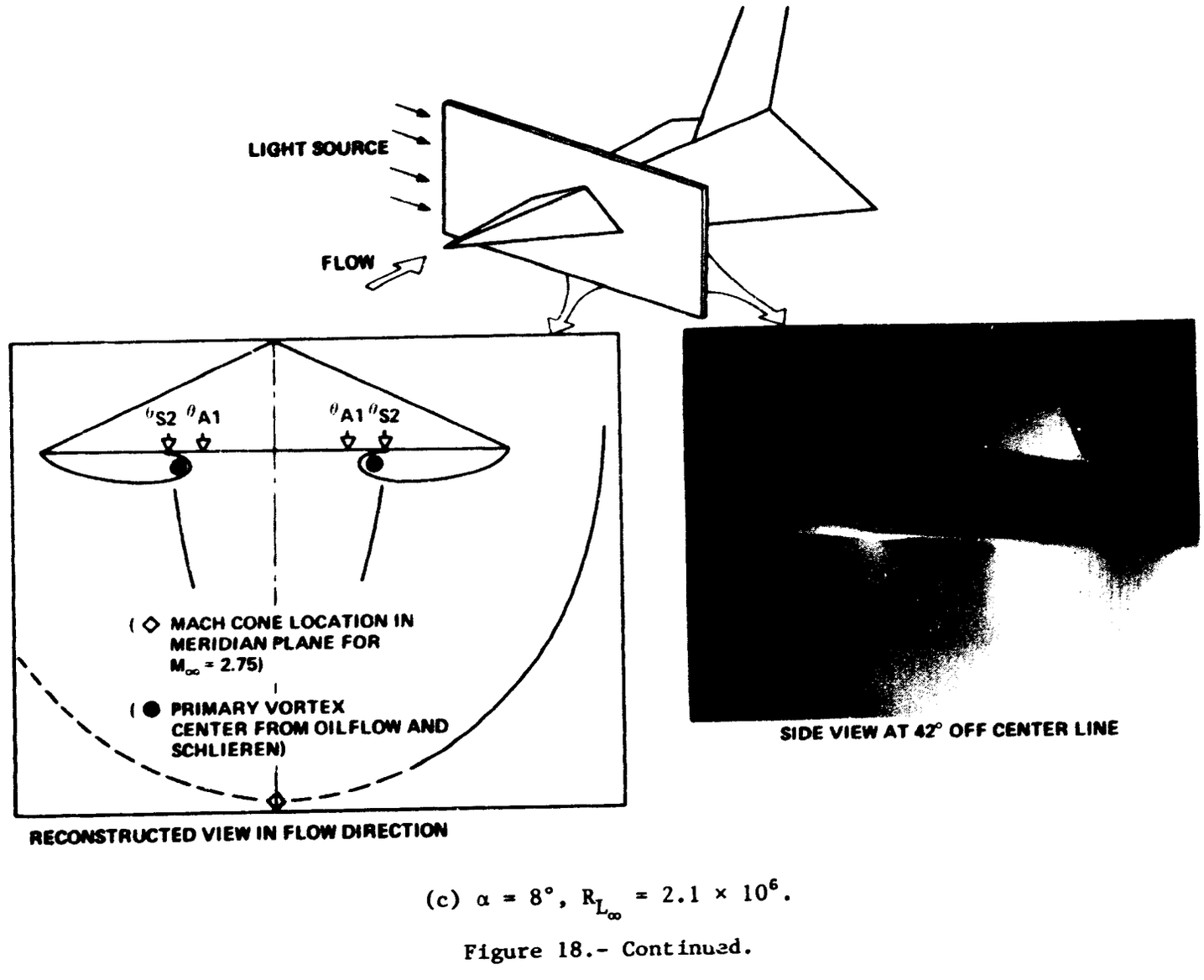

(c) $\alpha = 8°$, $R_{L_\infty} = 2.1 \times 10^6$.

Figure 18.- Continued.

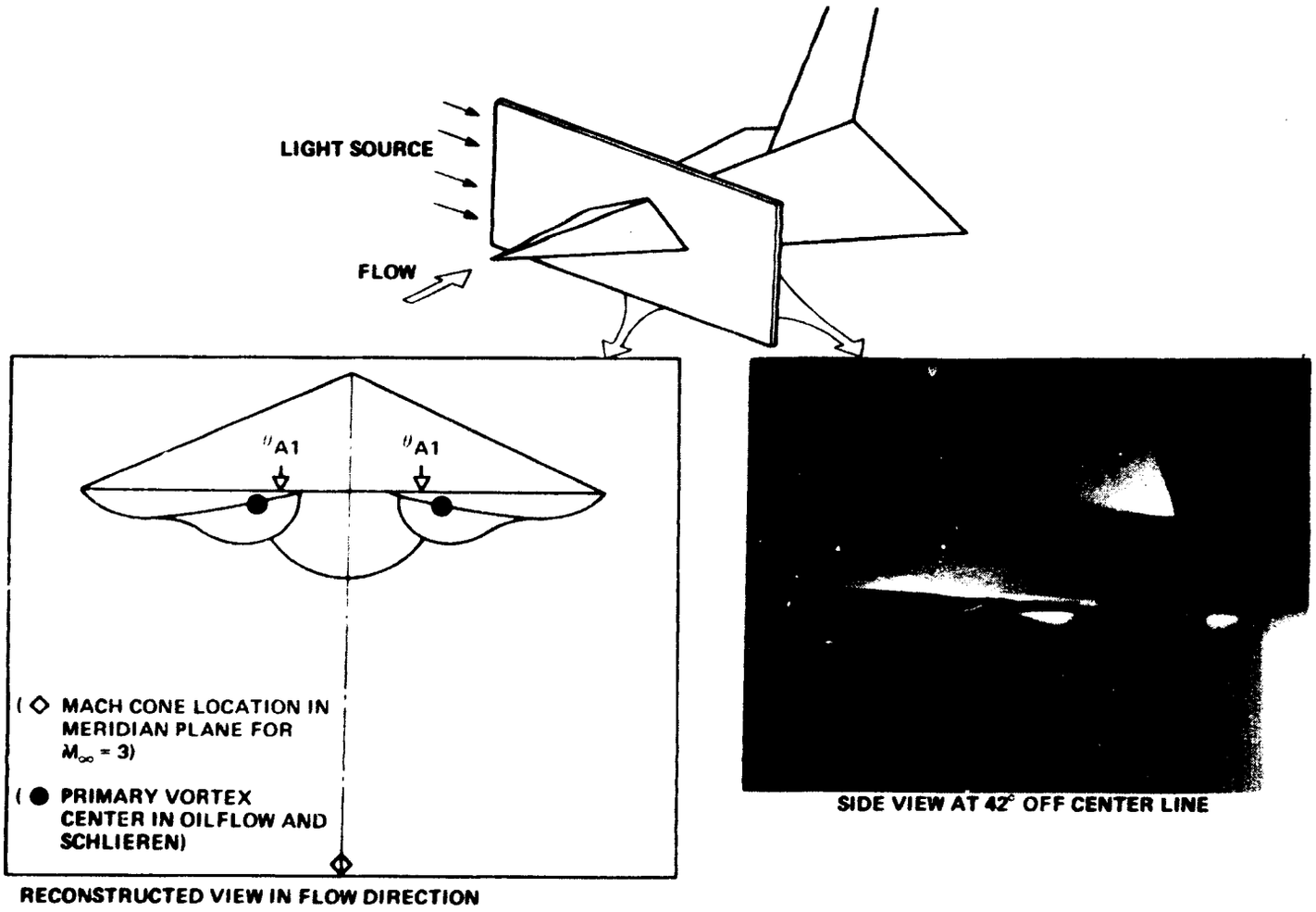

(d) $\alpha = 8°$, $R_{L_\infty} = 25 \times 10^6$.

Figure 18.- Concluded.

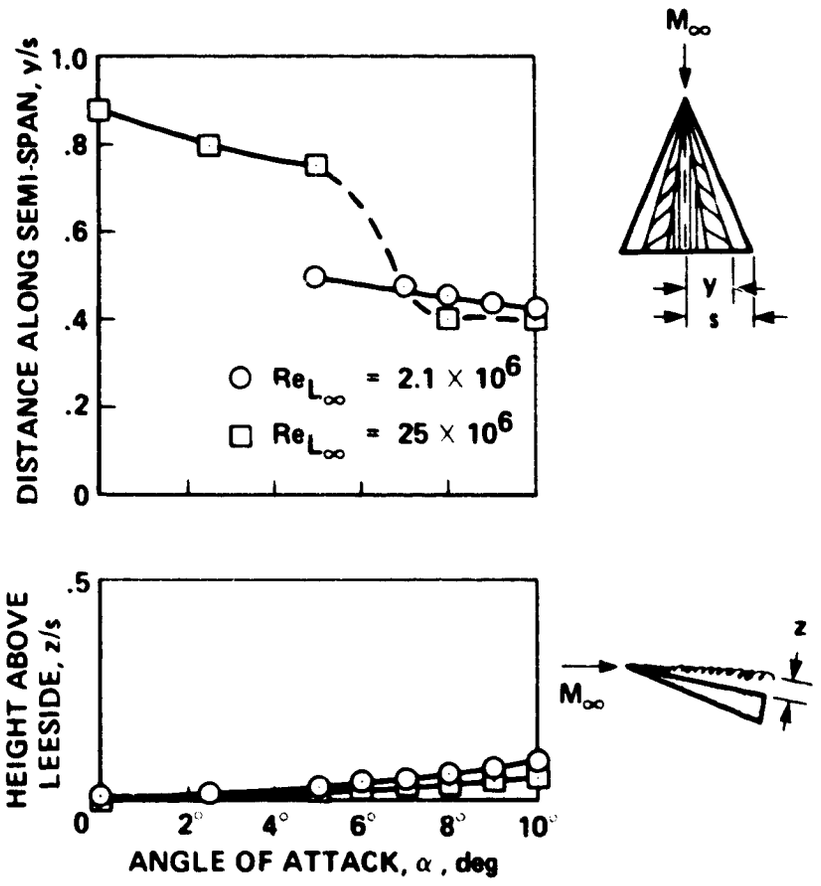

Figure 19.- Separation line and position of primary vortex above delta wing, M_∞ = 3.

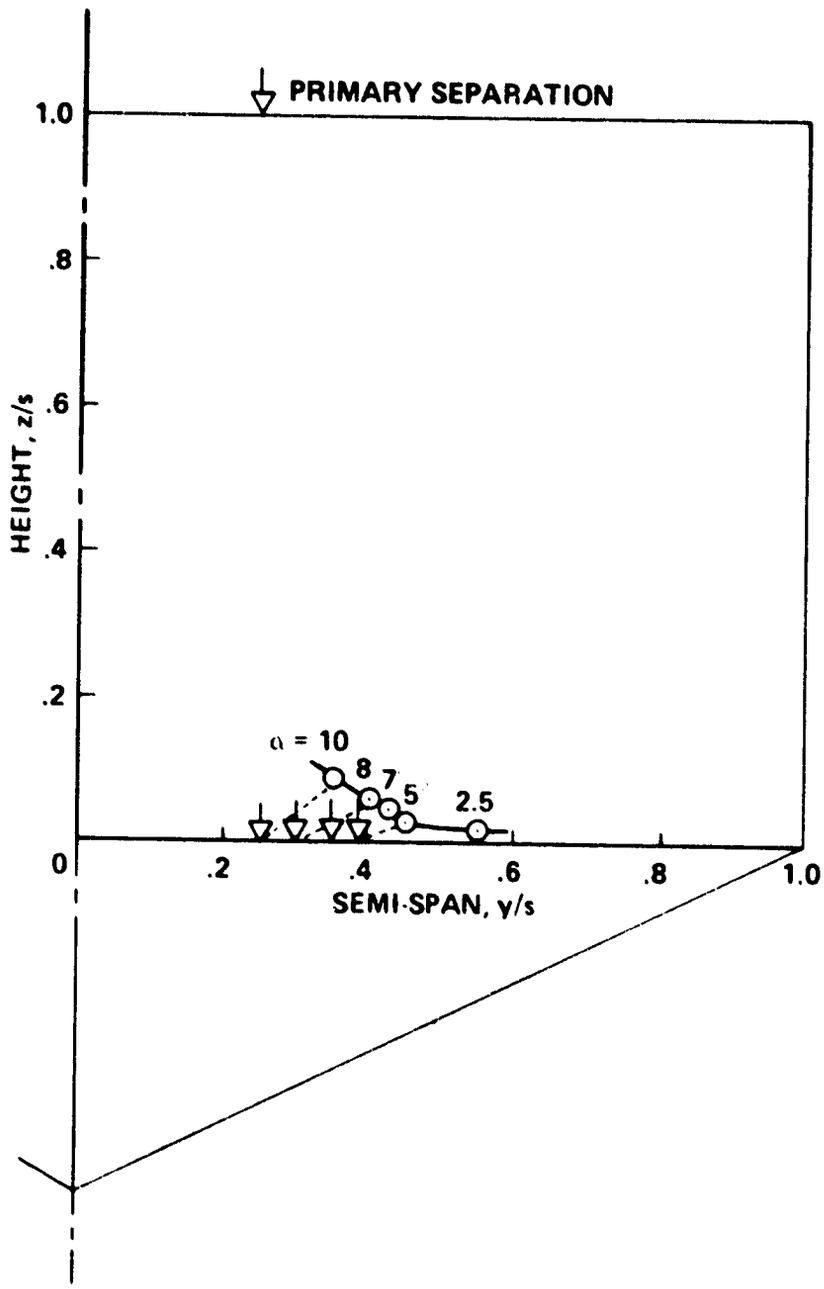

(a) $R_{L_\infty} = 2 \times 10^6$.

Figure 20.- Primary vortex position above leeward side of delta wing, $M_\infty = 3$.

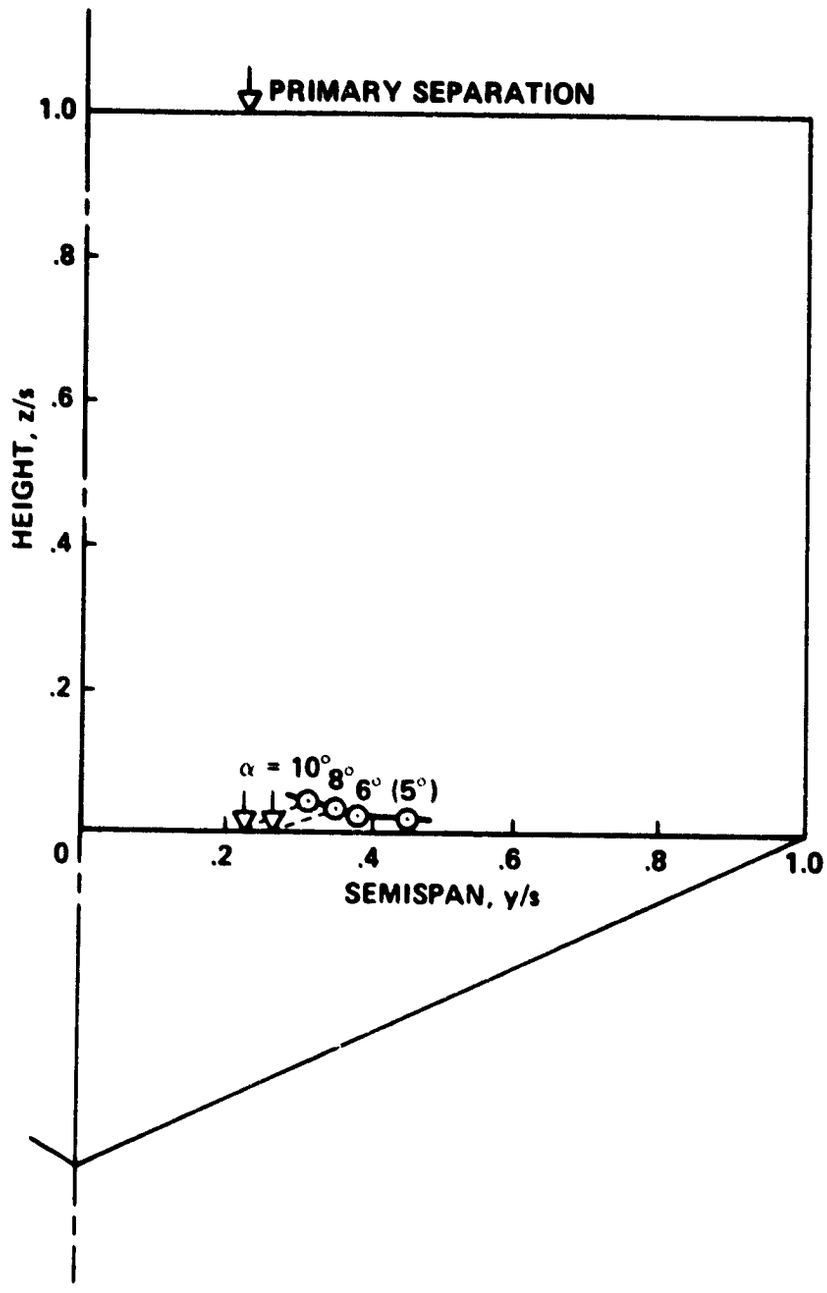

(b) $R_{L_\infty} = 25 \times 10^6$.

Figure 20.- Concluded.

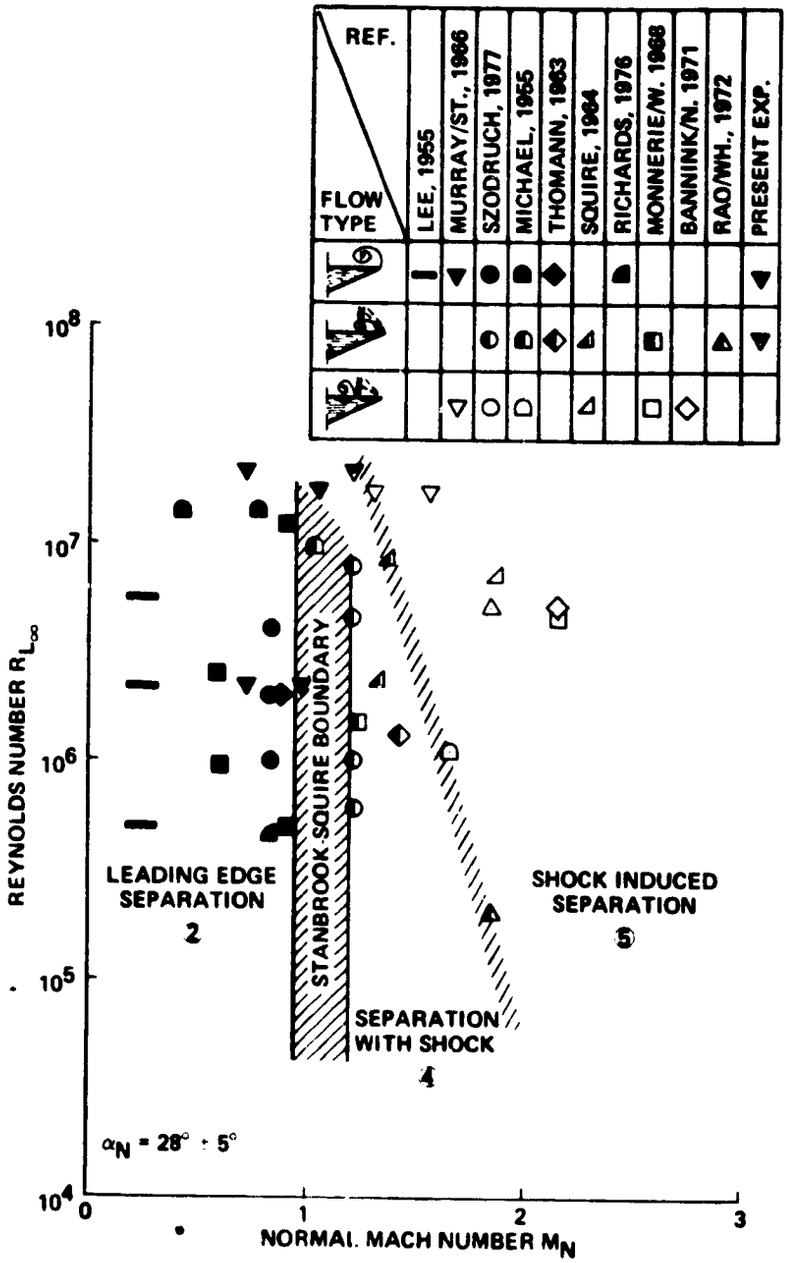

Figure 21.- Influence of Reynolds number on flow types and boundaries at constant α_N.

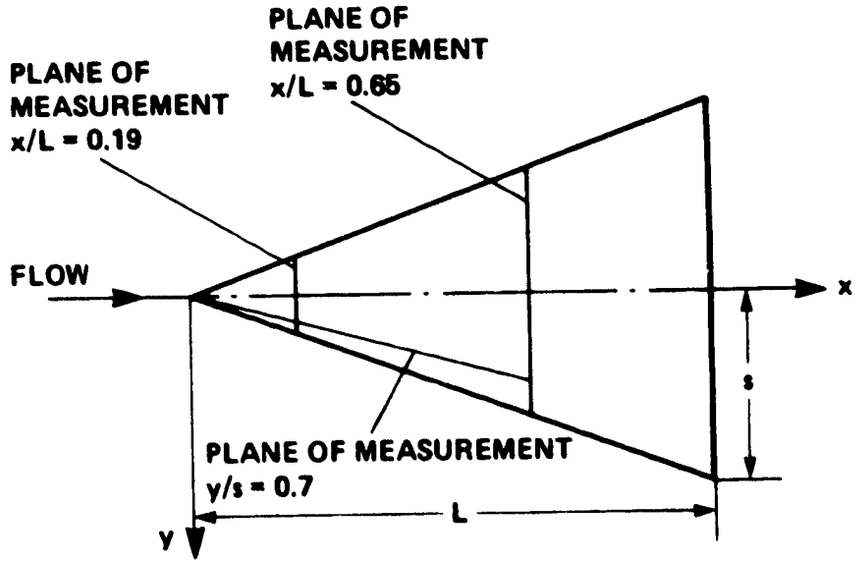

Figure 22.- Static pressure orifice location on leeward side of delta wing.

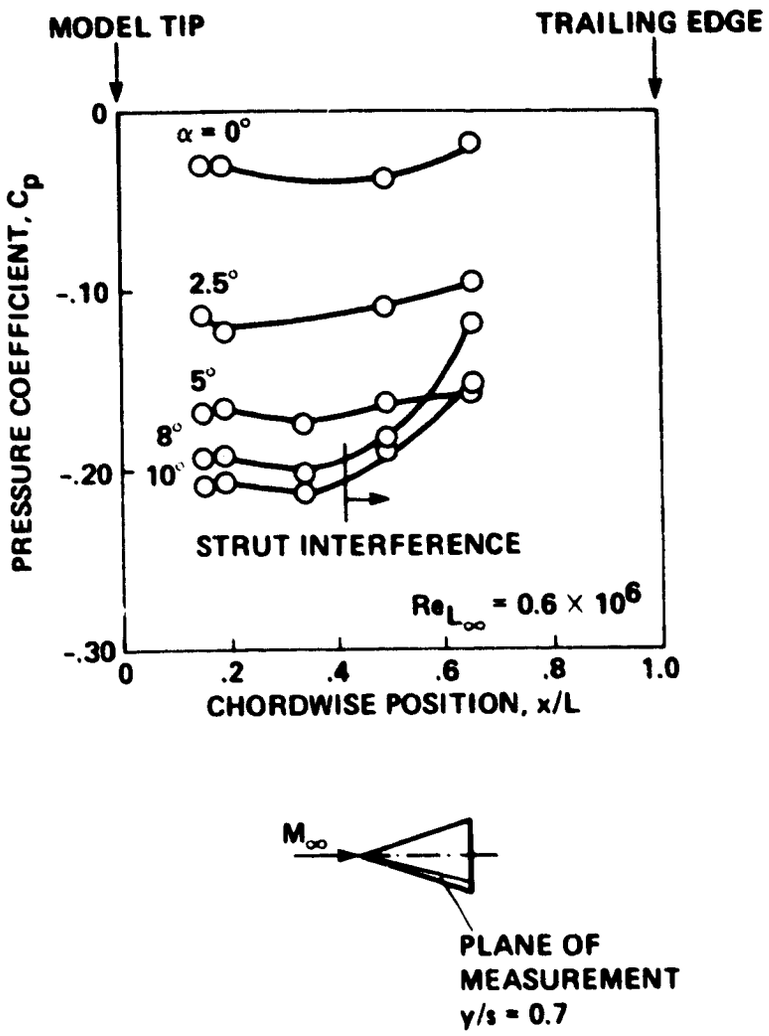

(a) Conical line at y/s = 0.7.

Figure 23.- Pressure distribution over the leeward side at M_∞ = 2 and R_{L_∞} = 0.6 × 10^6.

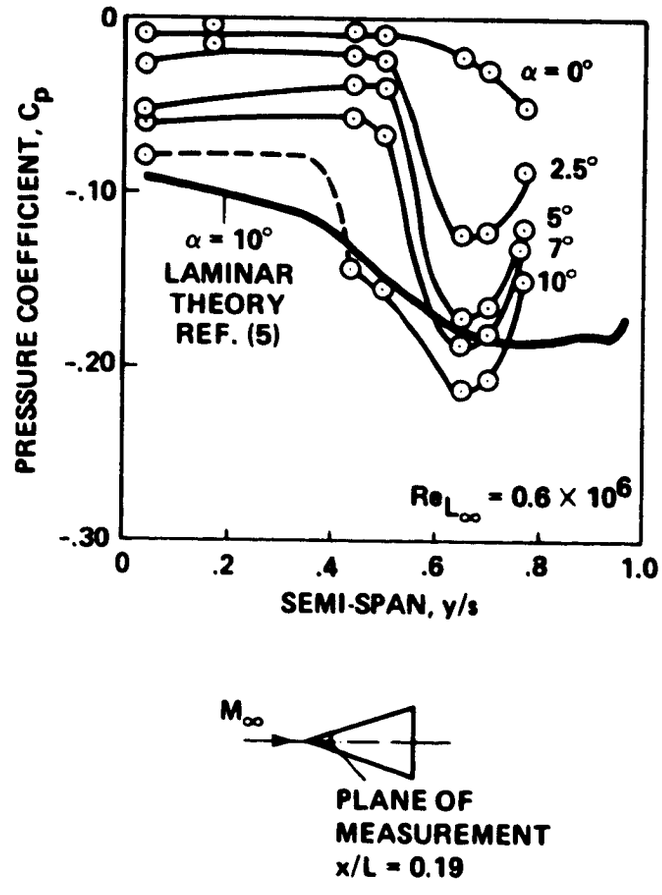

(b) Cross line at x/L = 0.19.

Figure 23.- Continued.

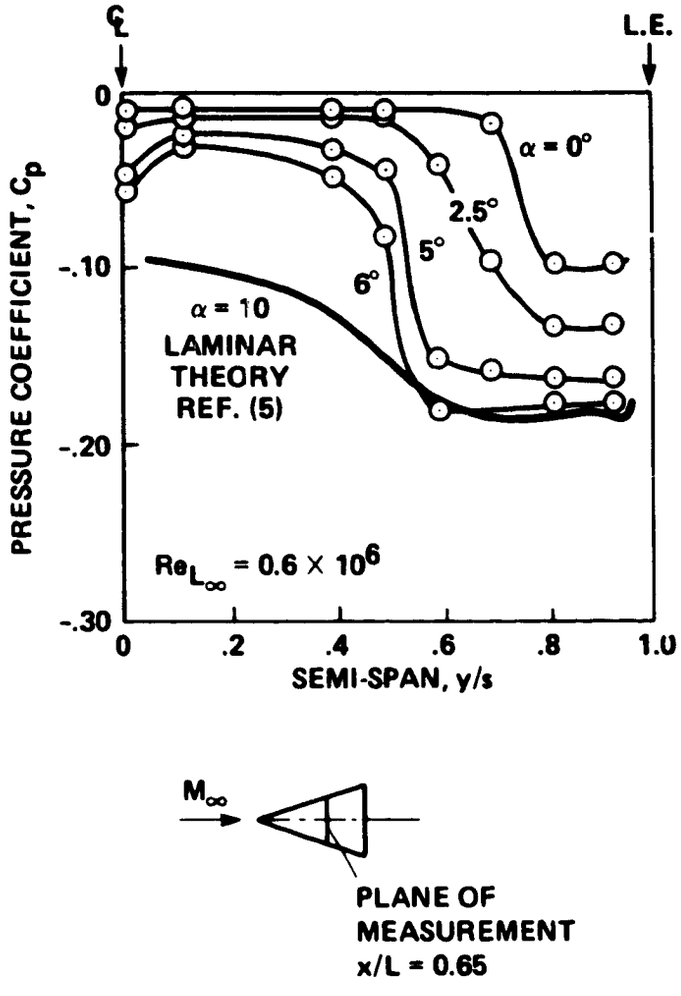

(c) Cross line at x/L = 0.65.

Figure 23.- Concluded.

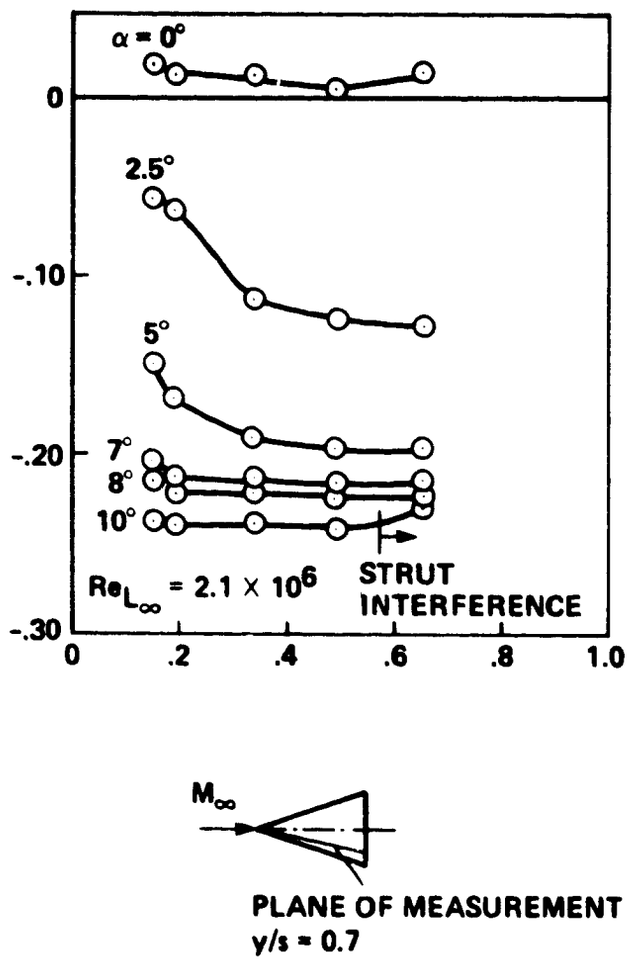

(a) Conical line at y/L = 0.7.

Figure 24.- Pressure distribution over the leeward side at $M_\infty = 2$ and $R_{L_\infty} = 2.1 \times 10^6$.

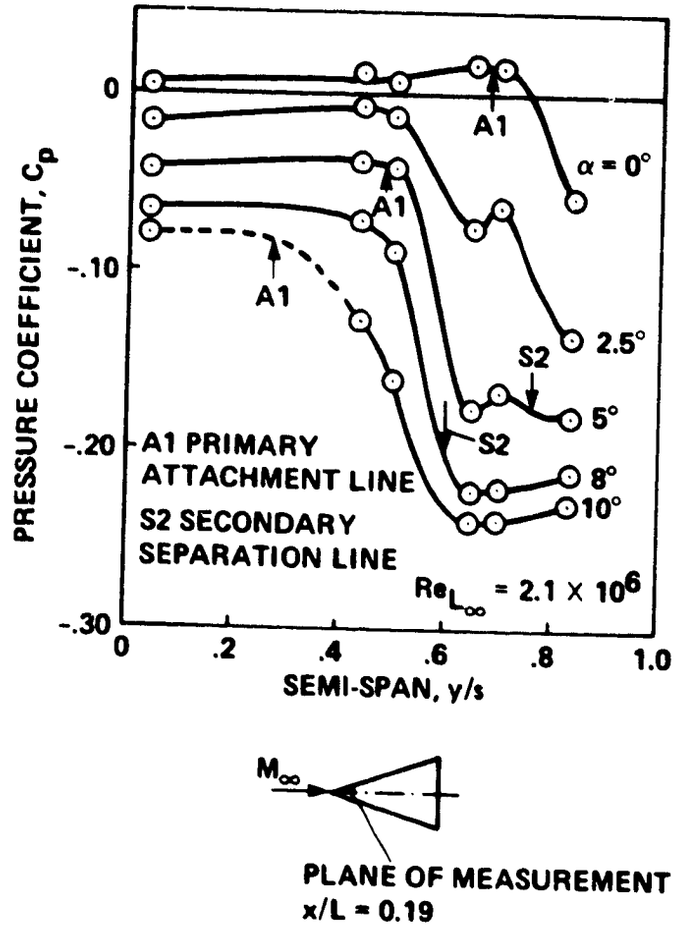

(b) Cross line at x/L = 0.19.

Figure 24.- Continued.

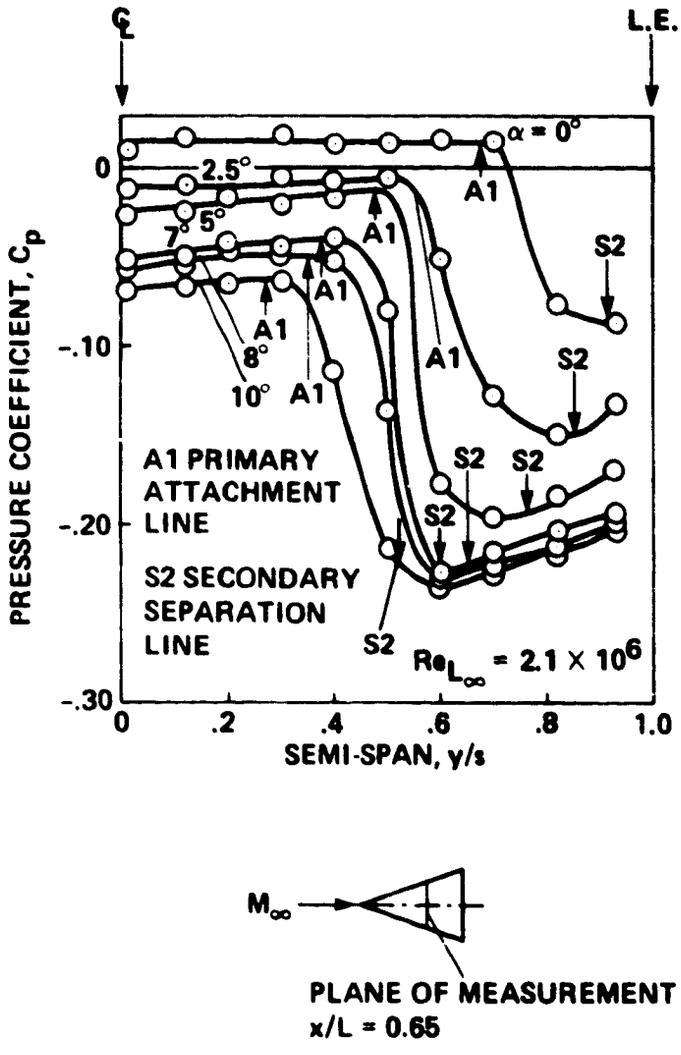

(c) Cross line at x/L = 0.65.

Figure 24.- Concluded.

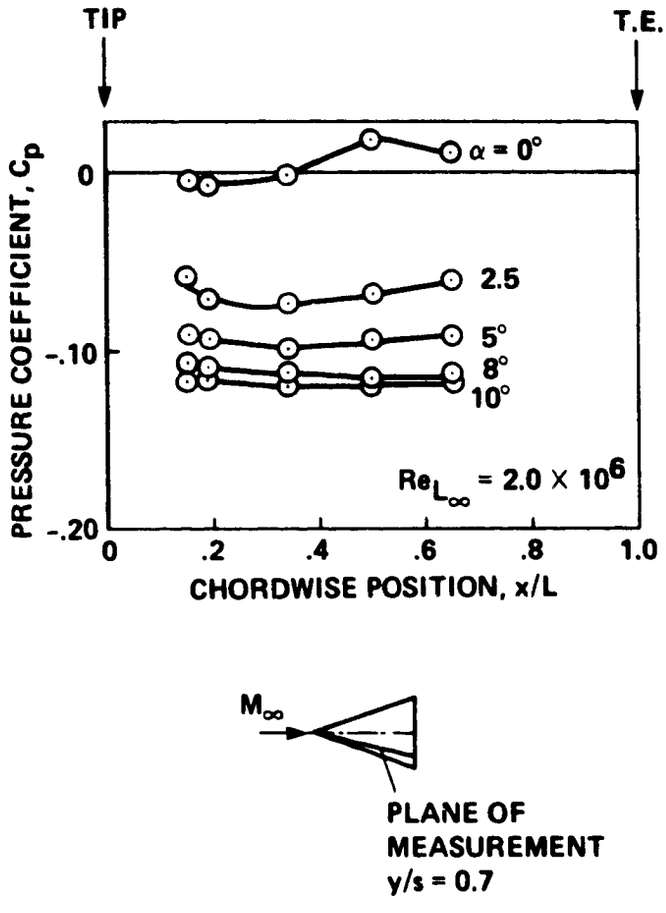

(a) Conical line at y/s = 0.7.

Figure 25.- Pressure distribution over the leeward side at M_∞ = 3 and R_{L_∞} = 2.0 × 10^6.

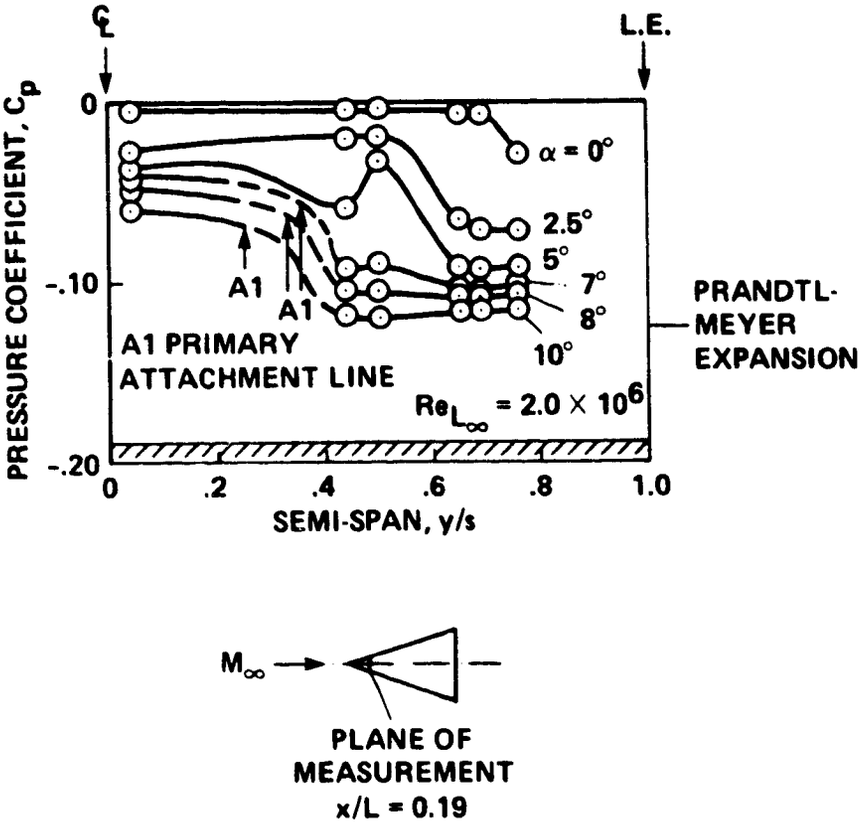

(b) Cross line at x/L = 0.19.

Figure 25.- Continued.

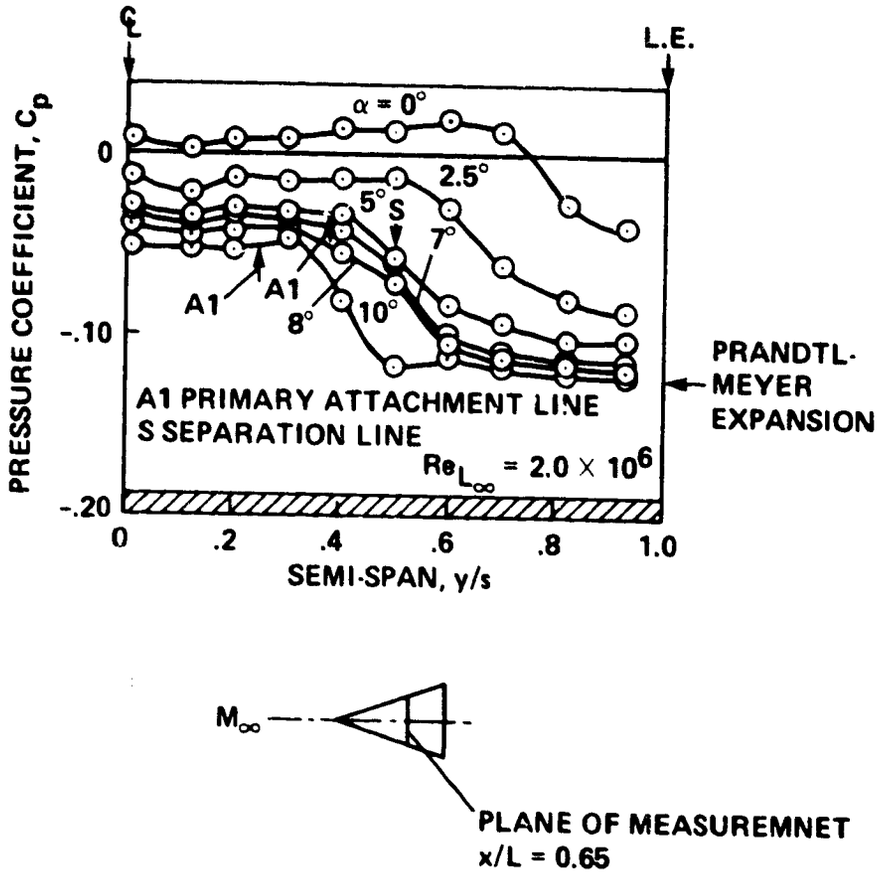

(c) Cross line at x/L = 0.65.

Figure 25.- Concluded.

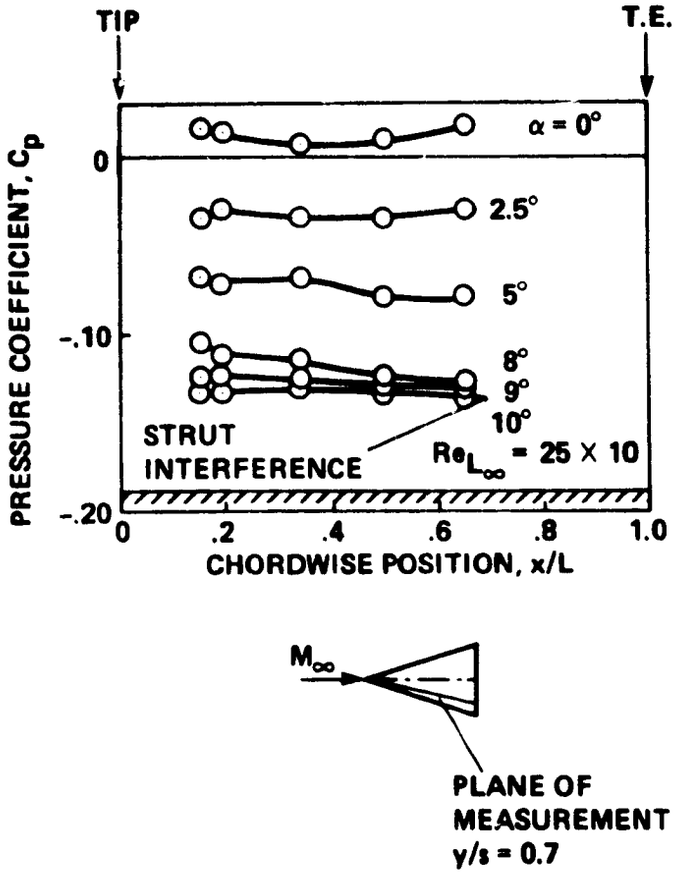

(a) Conical line at $y/s = 0.7$.

Figure 26.- Pressure distribution over the leeward side at $M_\infty = 3$ and $R_{L_\infty} = 25 \times 10^6$.

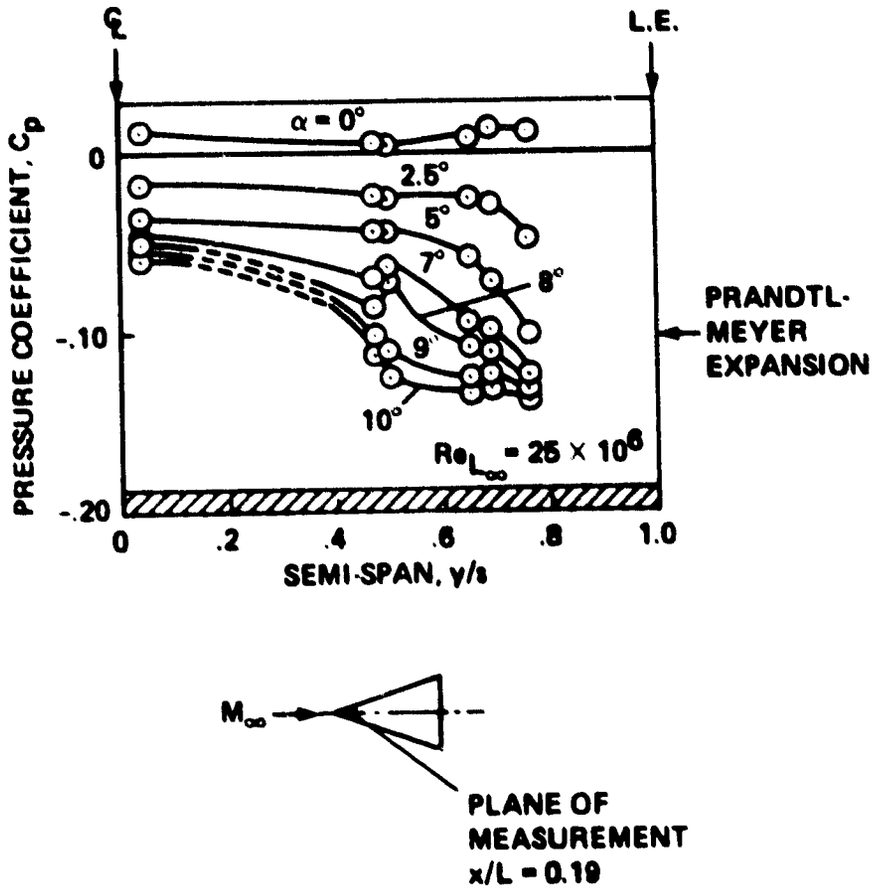

(b) Cross line at x/L = 0.19.

Figure 26.- Continued.

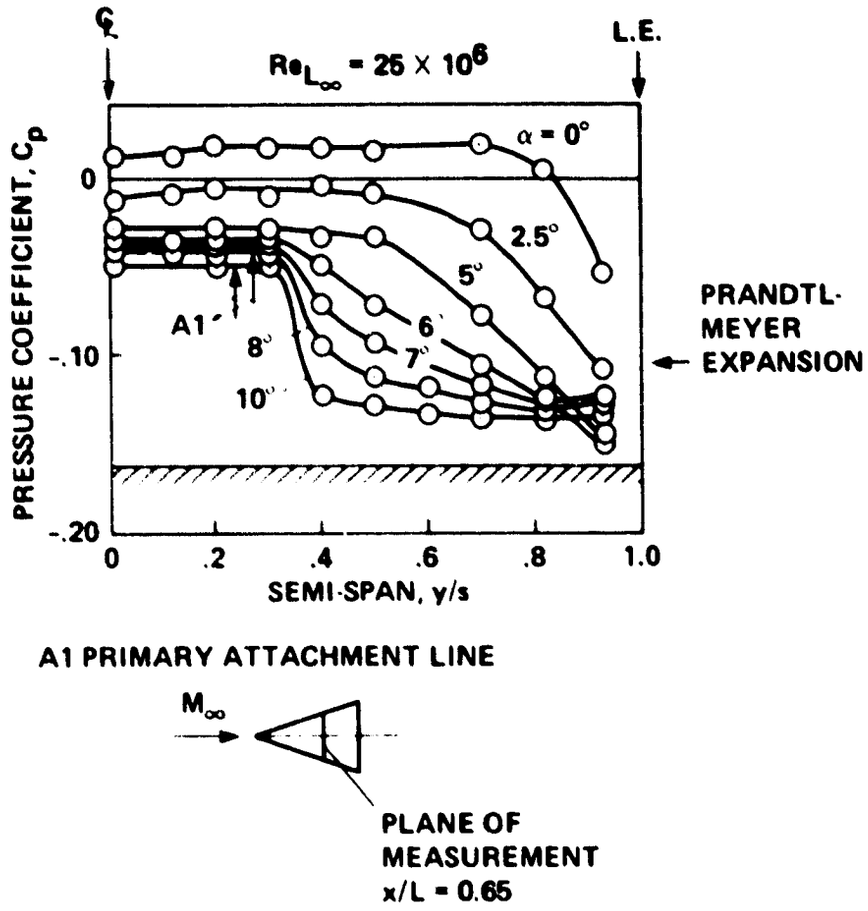

(c) Cross line at x/L = 0.65.

Figure 26.- Concluded.

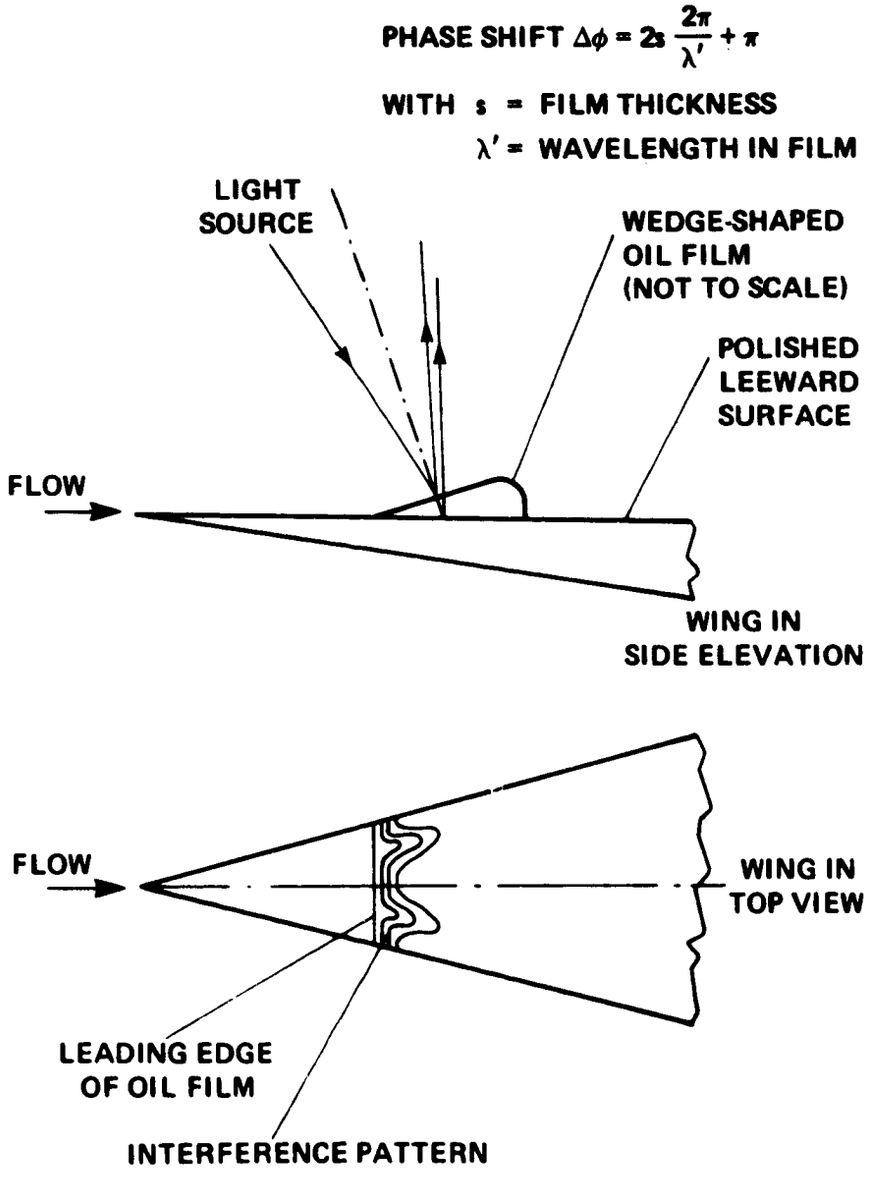

Figure 27.- Schematics of reflection on thin films.

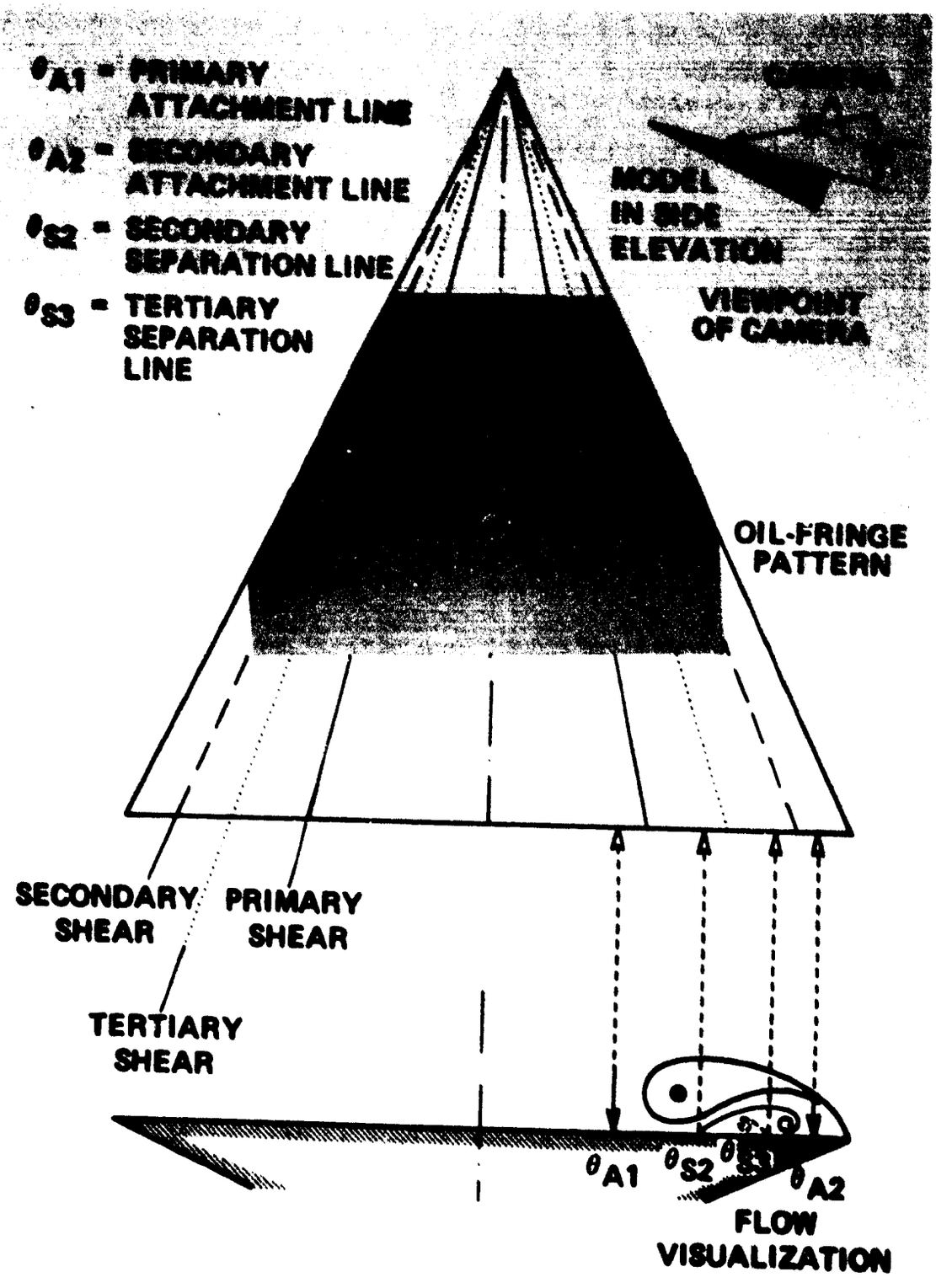

(a) $M_\infty = 2$.

Figure 28.- Shear stress fringe pattern on leeward side of delta wing at $\alpha = 8°$ and $R_{l_\infty} = 2.1 \times 10^6$.

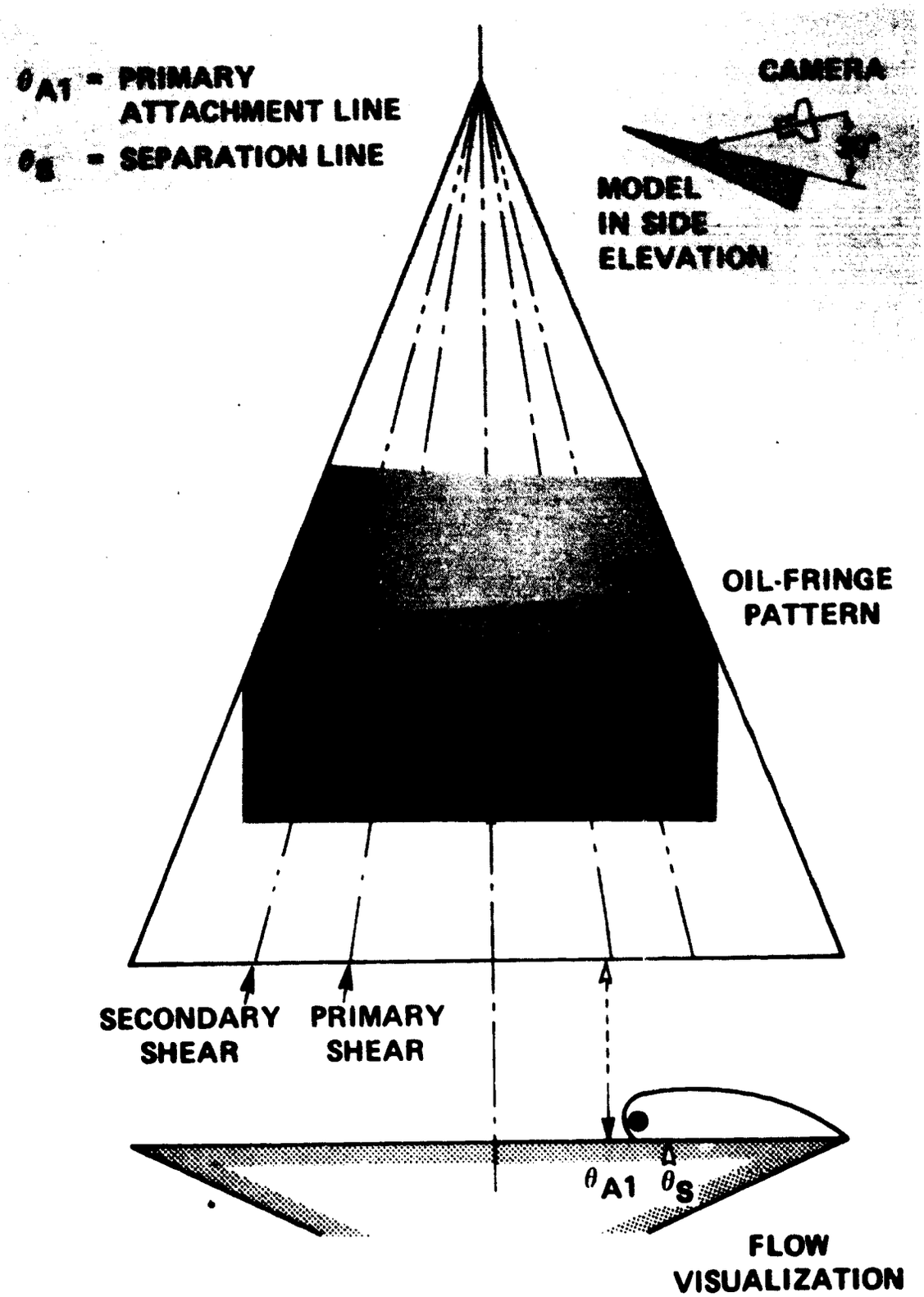

(b) $M_\infty = 3$.

Figure 28.- Concluded.